Measurement of single muons at forward rapidity in $p + p$ collisions at $\sqrt{s} = 200$ GeV and implications for charm production

S. S. Adler,[5] S. Afanasiev,[17] C. Aidala,[5] N. N. Ajitanand,[43] Y. Akiba,[20,38] J. Alexander,[43] R. Amirikas,[12] L. Aphecetche,[45] S. H. Aronson,[5] R. Averbeck,[44] T. C. Awes,[35] R. Azmoun,[44] V. Babintsev,[15] A. Baldisseri,[10] K. N. Barish,[6] P. D. Barnes,[27] B. Bassalleck,[33] S. Bathe,[30] S. Batsouli,[9] V. Baublis,[37] A. Bazilevsky,[39,15] S. Belikov,[16,15,*] Y. Berdnikov,[40] S. Bhagavatula,[16] J. G. Boissevain,[27] H. Borel,[10] S. Borenstein,[25] M. L. Brooks,[27] D. S. Brown,[34] N. Bruner,[33] D. Bucher,[30] H. Buesching,[30] V. Bumazhnov,[15] G. Bunce,[5,39] J. M. Burward-Hoy,[26,44] S. Butsyk,[44] X. Camard,[45] J.-S. Chai,[18] P. Chand,[4] W. C. Chang,[2] S. Chernichenko,[15] C. Y. Chi,[9] J. Chiba,[20] M. Chiu,[9] I. J. Choi,[52] J. Choi,[19] R. K. Choudhury,[4] T. Chujo,[5] V. Cianciolo,[35] Y. Cobigo,[10] B. A. Cole,[9] P. Constantin,[16] D. d'Enterria,[45] G. David,[5] H. Delagrange,[45] A. Denisov,[15] A. Deshpande,[39] E. J. Desmond,[5] A. Devismes,[44] O. Dietzsch,[41] O. Drapier,[25] A. Drees,[44] K. A. Drees,[5] R. du Rietz,[29] A. Durum,[15] D. Dutta,[4] Y. V. Efremenko,[35] K. El Chenawi,[49] A. Enokizono,[14] H. En'yo,[38,39] S. Esumi,[48] L. Ewell,[5] D. E. Fields,[33,39] F. Fleuret,[25] S. L. Fokin,[23] B. D. Fox,[39] Z. Fraenkel,[51] J. E. Frantz,[9] A. Franz,[5] A. D. Frawley,[12] S.-Y. Fung,[6] S. Garpman,[29,*] T. K. Ghosh,[49] A. Glenn,[46] G. Gogiberidze,[46] M. Gonin,[25] J. Gosset,[10] Y. Goto,[39] R. Granier de Cassagnac,[25] N. Grau,[16] S. V. Greene,[49] M. Grosse Perdekamp,[39] W. Guryn,[5] H.-Å. Gustafsson,[29] T. Hachiya,[14] J. S. Haggerty,[5] H. Hamagaki,[8] A. G. Hansen,[27] E. P. Hartouni,[26] M. Harvey,[5] R. Hayano,[8] N. Hayashi,[38] X. He,[13] M. Heffner,[26] T. K. Hemmick,[44] J. M. Heuser,[44] M. Hibino,[50] J. C. Hill,[16] W. Holzmann,[43] K. Homma,[14] B. Hong,[22] A. Hoover,[34] D. Hornback,[46] T. Ichihara,[38,39] V. V. Ikonnikov,[23] K. Imai,[24,38] D. Isenhower,[1] M. Ishihara,[38] M. Issah,[43] A. Isupov,[17] B. V. Jacak,[44] W. Y. Jang,[22] Y. Jeong,[19] J. Jia,[44] O. Jinnouchi,[38] B. M. Johnson,[5] S. C. Johnson,[26] K. S. Joo,[31] D. Jouan,[36] S. Kametani,[8,50] N. Kamihara,[38,47] J. H. Kang,[52] S. S. Kapoor,[4] K. Katou,[50] S. Kelly,[9] B. Khachaturov,[51] A. Khanzadeev,[37] J. Kikuchi,[50] D. H. Kim,[31] D. J. Kim,[52] D. W. Kim,[19] E. Kim,[42] G.-B. Kim,[25] H. J. Kim,[52] E. Kistenev,[5] A. Kiyomichi,[48] K. Kiyoyama,[32] C. Klein-Boesing,[30] H. Kobayashi,[38,39] L. Kochenda,[37] V. Kochetkov,[15] D. Koehler,[33] T. Kohama,[14] M. Kopytine,[44] D. Kotchetkov,[6] A. Kozlov,[51] P. J. Kroon,[5] C. H. Kuberg,[1,27,*] K. Kurita,[39] Y. Kuroki,[48] M. J. Kweon,[22] Y. Kwon,[52] G. S. Kyle,[34] R. Lacey,[43] V. Ladygin,[17] J. G. Lajoie,[16] A. Lebedev,[16,23] S. Leckey,[44] D. M. Lee,[27] S. Lee,[19] M. J. Leitch,[27] X. H. Li,[6] H. Lim,[42] A. Litvinenko,[17] M. X. Liu,[27] Y. Liu,[36] C. F. Maguire,[49] Y. I. Makdisi,[5] A. Malakhov,[17] V. I. Manko,[23] Y. Mao,[7,38] G. Martinez,[45] M. D. Marx,[44] H. Masui,[48] F. Matathias,[44] T. Matsumoto,[8,50] P. L. McGaughey,[27] E. Melnikov,[15] F. Messer,[44] Y. Miake,[48] J. Milan,[43] T. E. Miller,[49] A. Milov,[44,51] S. Mioduszewski,[5] R. E. Mischke,[27] G. C. Mishra,[13] J. T. Mitchell,[5] A. K. Mohanty,[4] D. P. Morrison,[5] J. M. Moss,[27] F. Mühlbacher,[44] D. Mukhopadhyay,[51] M. Muniruzzaman,[6] J. Murata,[38,39] S. Nagamiya,[20] J. L. Nagle,[9] T. Nakamura,[14] B. K. Nandi,[6] M. Nara,[48] J. Newby,[46] P. Nilsson,[29] A. S. Nyanin,[23] J. Nystrand,[29] E. O'Brien,[5] C. A. Ogilvie,[16] H. Ohnishi,[5,38] I. D. Ojha,[3,49] K. Okada,[38] M. Ono,[48] V. Onuchin,[15] A. Oskarsson,[29] I. Otterlund,[29] K. Oyama,[8] K. Ozawa,[8] D. Pal,[51] A. P. T. Palounek,[27] V. Pantuev,[44] V. Papavassiliou,[34] J. Park,[42] A. Parmar,[33] S. F. Pate,[34] T. Peitzmann,[30] J.-C. Peng,[27] V. Peresedov,[17] C. Pinkenburg,[5] R. P. Pisani,[5] F. Plasil,[35] M. L. Purschke,[5] A. K. Purwar,[44] J. Rak,[16] I. Ravinovich,[51] K. F. Read,[35,46] M. Reuter,[44] K. Reygers,[30] V. Riabov,[37,40] Y. Riabov,[37] G. Roche,[28] A. Romana,[25,*] M. Rosati,[16] P. Rosnet,[28] S. S. Ryu,[52] M. E. Sadler,[1] N. Saito,[38,39] T. Sakaguchi,[8,50] M. Sakai,[32] S. Sakai,[48] V. Samsonov,[37] L. Sanfratello,[33] R. Santo,[30] H. D. Sato,[24,38] S. Sato,[5,48] S. Sawada,[20] Y. Schutz,[45] V. Semenov,[15] R. Seto,[6] M. R. Shaw,[1,27] T. K. Shea,[5] T.-A. Shibata,[38,47] K. Shigaki,[14,20] T. Shiina,[27] C. L. Silva,[41] D. Silvermyr,[27,29] K. S. Sim,[22] C. P. Singh,[3] V. Singh,[3] M. Sivertz,[5] A. Soldatov,[15] R. A. Soltz,[26] W. E. Sondheim,[27] S. P. Sorensen,[46] I. V. Sourikova,[5] F. Staley,[10] P. W. Stankus,[35] E. Stenlund,[29] M. Stepanov,[34] A. Ster,[21] S. P. Stoll,[5] T. Sugitate,[14] J. P. Sullivan,[27] E. M. Takagui,[41] A. Taketani,[38,39] M. Tamai,[50] K. H. Tanaka,[20] Y. Tanaka,[32] K. Tanida,[38] M. J. Tannenbaum,[5] P. Tarján,[11] J. D. Tepe,[1,27] T. L. Thomas,[33] J. Tojo,[24,38] H. Torii,[24,38] R. S. Towell,[1] I. Tserruya,[51] H. Tsuruoka,[48] S. K. Tuli,[3] H. Tydesjö,[29] N. Tyurin,[15] H. W. van Hecke,[27] J. Velkovska,[5,44] M. Velkovsky,[44] V. Veszprémi,[11] L. Villatte,[46] A. A. Vinogradov,[23] M. A. Volkov,[23] E. Vznuzdaev,[37] X. R. Wang,[13] Y. Watanabe,[38,39] S. N. White,[5] F. K. Wohn,[16] C. L. Woody,[5] W. Xie,[6] Y. Yang,[7] A. Yanovich,[15] S. Yokkaichi,[38,39] G. R. Young,[35] I. E. Yushmanov,[23] W. A. Zajc,[9,†] C. Zhang,[9] S. Zhou,[7] S. J. Zhou,[51] and L. Zolin[17]

(PHENIX Collaboration)

[1]*Abilene Christian University, Abilene, Texas 79699, USA*
[2]*Institute of Physics, Academia Sinica, Taipei 11529, Taiwan*
[3]*Department of Physics, Banaras Hindu University, Varanasi 221005, India*
[4]*Bhabha Atomic Research Centre, Bombay 400 085, India*

 © 2007 The American Physical Society

[5]*Brookhaven National Laboratory, Upton, New York 11973-5000, USA*
[6]*University of California-Riverside, Riverside, California 92521, USA*
[7]*China Institute of Atomic Energy (CIAE), Beijing, People's Republic of China*
[8]*Center for Nuclear Study, Graduate School of Science, University of Tokyo, 7-3-1 Hongo, Bunkyo, Tokyo 113-0033, Japan*
[9]*Columbia University, New York, New York 10027*
and Nevis Laboratories, Irvington, New York 10533, USA
[10]*Dapnia, CEA Saclay, F-91191, Gif-sur-Yvette, France*
[11]*Debrecen University, H-4010 Debrecen, Egyetem tér 1, Hungary*
[12]*Florida State University, Tallahassee, Florida 32306, USA*
[13]*Georgia State University, Atlanta, Georgia 30303, USA*
[14]*Hiroshima University, Kagamiyama, Higashi-Hiroshima 739-8526, Japan*
[15]*Institute for High Energy Physics (IHEP), Protvino, Russia*
[16]*Iowa State University, Ames, Iowa 50011, USA*
[17]*Joint Institute for Nuclear Research, 141980 Dubna, Moscow Region, Russia*
[18]*KAERI, Cyclotron Application Laboratory, Seoul, South Korea*
[19]*Kangnung National University, Kangnung 210-702, South Korea*
[20]*KEK, High Energy Accelerator Research Organization, Tsukuba-shi, Ibaraki-ken 305-0801, Japan*
[21]*KFKI Research Institute for Particle and Nuclear Physics (RMKI), H-1525 Budapest 114, POBox 49, Hungary*
[22]*Korea University, Seoul, 136-701, Korea*
[23]*Russian Research Center "Kurchatov Institute", Moscow, Russia*
[24]*Kyoto University, Kyoto 606-8502, Japan*
[25]*Laboratoire Leprince-Ringuet, Ecole Polytechnique, CNRS-IN2P3, Route de Saclay, F-91128, Palaiseau, France*
[26]*Lawrence Livermore National Laboratory, Livermore, California 94550, USA*
[27]*Los Alamos National Laboratory, Los Alamos, New Mexico 87545, USA*
[28]*LPC, Université Blaise Pascal, CNRS-IN2P3, Clermont-Fd, 63177 Aubiere Cedex, France*
[29]*Department of Physics, Lund University, Box 118, SE-221 00 Lund, Sweden*
[30]*Institut für Kernphysik, University of Muenster, D-48149 Muenster, Germany*
[31]*Myongji University, Yongin, Kyonggido 449-728, Korea*
[32]*Nagasaki Institute of Applied Science, Nagasaki-shi, Nagasaki 851-0193, Japan*
[33]*University of New Mexico, Albuquerque, New Mexico 87131, USA*
[34]*New Mexico State University, Las Cruces, New Mexico 88003, USA*
[35]*Oak Ridge National Laboratory, Oak Ridge, Tennessee 37831, USA*
[36]*IPN-Orsay, Universite Paris Sud, CNRS-IN2P3, BP1, F-91406, Orsay, France*
[37]*PNPI, Petersburg Nuclear Physics Institute, Gatchina, Russia*
[38]*RIKEN (The Institute of Physical and Chemical Research), Wako, Saitama 351-0198, Japan*
[39]*RIKEN BNL Research Center, Brookhaven National Laboratory, Upton, New York 11973-5000, USA*
[40]*St. Petersburg State Technical University, St. Petersburg, Russia*
[41]*Universidade de São Paulo, Instituto de Física, Caixa Postal 66318, São Paulo CEP05315-970, Brazil*
[42]*System Electronics Laboratory, Seoul National University, Seoul, South Korea*
[43]*Chemistry Department, Stony Brook University, SUNY, Stony Brook, New York 11794-3400, USA*
[44]*Department of Physics and Astronomy, Stony Brook University, SUNY, Stony Brook, New York 11794, USA*
[45]*SUBATECH (Ecole des Mines de Nantes, CNRS-IN2P3, Université de Nantes) BP 20722 - 44307, Nantes, France*
[46]*University of Tennessee, Knoxville, Tennessee 37996, USA*
[47]*Department of Physics, Tokyo Institute of Technology, Tokyo, 152-8551, Japan*
[48]*Institute of Physics, University of Tsukuba, Tsukuba, Ibaraki 305, Japan*
[49]*Vanderbilt University, Nashville, Tennessee 37235, USA*
[50]*Waseda University, Advanced Research Institute for Science and Engineering, 17 Kikui-cho, Shinjuku-ku, Tokyo 162-0044, Japan*
[51]*Weizmann Institute, Rehovot 76100, Israel*
[52]*Yonsei University, IPAP, Seoul 120-749, Korea*

(Received 18 September 2006; revised manuscript received 21 May 2007; published 13 November 2007)

Muon production at forward rapidity ($1.5 \leq |\eta| \leq 1.8$) has been measured by the PHENIX experiment over the transverse momentum range $1 \leq p_T \leq 3$ GeV/c in $\sqrt{s} = 200$ GeV $p + p$ collisions at the Relativistic Heavy Ion Collider. After statistically subtracting contributions from light hadron decays an excess remains which is attributed to the semileptonic decays of hadrons carrying heavy flavor, i.e. charm quarks or, at high p_T, bottom quarks. The resulting muon spectrum from heavy flavor decays is compared to PYTHIA and a next-to-leading-order perturbative QCD calculation. PYTHIA is used to determine the

[*]Deceased.
[†]PHENIX Spokesperson; zajc@nevis.columbia.edu

charm quark spectrum that would produce the observed muon excess. The corresponding differential cross section for charm quark production at forward rapidity is determined to be $d\sigma_{c\bar{c}}/dy|_{y=1.6} = 0.243 \pm 0.013(\text{stat.}) \pm 0.105(\text{data syst.}) \,^{+0.049}_{-0.087}\,(\text{PYTHIA syst.})$ mb.

DOI: 10.1103/PhysRevD.76.092002 PACS numbers: 13.85.Qk, 13.20.Fc, 13.20.He, 25.75.Dw

I. INTRODUCTION

Measurements of heavy quark production in proton-proton ($p + p$) interactions at collider energies serve as important tests for perturbative quantum chromodynamics (pQCD). Bottom production at the Tevatron collider ($\sqrt{s} =$ 1.8 and 1.96 TeV) [1,2] is reasonably well described by a recent fixed order next-to-leading logarithm (FONLL) calculation [3–5]. Charm production at FNAL, which has only been measured at relatively high p_T (> 5 GeV/c), is $\approx 50\%$ higher than the FONLL prediction [6]. However, theoretical and experimental uncertainties are large, such that significant disagreement between theory and data cannot be claimed.

Measurements at Brookhaven National Laboratory's Relativistic Heavy Ion Collider (RHIC), by both the PHENIX and STAR experiments, have provided a wealth of information on midrapidity open charm production in collisions at $\sqrt{s_{NN}} = 130$ GeV ($p + p$) and $\sqrt{s_{NN}} =$ 200 GeV ($p + p$, $d + Au$, and $Au + Au$) down to $p_T \approx$ 0.5 GeV/c. Semileptonic decay of produced charm quarks is the primary source of high p_T leptons after contributions from known (light hadron) sources are subtracted. Both PHENIX [7–16] and STAR [17,18] have made statistical measurements of charm production via single-electron spectra. STAR has also made a direct measurement of charm production through reconstruction of hadronic decay modes of D mesons [17]. In $p + p$ collisions at $\sqrt{s_{NN}} = 200$ GeV PHENIX finds $d\sigma_{c\bar{c}}/dy|_{y=0} = 0.123 \pm 0.012(\text{stat.}) \pm 0.045(\text{syst.})$ mb [13]. STAR finds a somewhat higher central value, $d\sigma_{c\bar{c}}/dy|_{y=0} = 0.30 \pm 0.04(\text{stat.}) \pm 0.09(\text{syst.})$ mb [17], but the two measurements are consistent within the stated uncertainties. Both measurements are noticeably (2–4 $\times$) higher than PYTHIA (a leading order pQCD event generator) [19] [see experimental references for specific parameter sets] and FONLL [20]. Again, quantitative disagreement cannot be established with current experimental and theoretical uncertainties. However, we note that there is some debate about whether charm quarks are heavy enough to be reliably treated by pQCD [21].

Such measurements also serve as an important baseline for charm production in proton-nucleus or deuteron-nucleus ($p + A$ or $d + A$), and nucleus-nucleus ($A + B$) collisions [22–25]. In the absence of any nuclear effects, charm production (since it is a pointlike process) is expected to scale with the number of binary nucleon-nucleon collisions (N_{coll}), which depends on the impact parameter of the nuclear collision and can be obtained from a Glauber calculation [26]. The degree of scaling for any given centrality bin is quantified by the nuclear modification factor:

$$R_{AB} = \frac{1}{N^{AB}_{\text{coll}}} \times \frac{dN^{AB}/dy}{dN^{pp}/dy}. \quad (1)$$

Deviations from this scaling ($R_{AB} \neq 1$) in $p + A$ or $d + A$ collisions quantify cold nuclear matter effects (such as initial state energy loss [27–32], and shadowing [33–37]). Any such deviation must be understood so that in $A + B$ collisions contributions to $R_{AB} \neq 1$ from hot nuclear matter effects (such as in-medium energy loss [[38] and references therein] and cold nuclear matter effects can be disentangled. In $d + Au$ collisions both PHENIX and STAR find little or no effect of cold nuclear matter on charm production ($R_{dAu} \approx 1$ over the measured lepton p_T [10,17]). This contrasts with measurements of open charm in $Au + Au$ collisions: although the *total* charm production appears to scale with N_{coll} [8], there is a strong suppression of lepton spectra for $p_T > 2$ GeV/c that increases with centrality [11,12,18]. Furthermore the elliptical flow of nonphotonic single electrons, as measured by PHENIX in $Au + Au$ collisions [14–16], implies that the charm quarks interact strongly with the created medium.

Finally, since the initial formation of open and closed charm are both sensitive to initial gluon densities [39,40], open charm production serves as an appropriate normalization for J/ψ production. The production of J/ψ mesons is expected to be sensitive to the production of a quark gluon plasma (QGP), should one be formed in $A + B$ collisions [41–46]. In order to understand J/ψ production differences in $A + B$ collisions compared to $p + p$ and $p + A$ collisions it is important to take into account any differences in the charm quark production in each of the different systems.

Until now, open charm measurements at RHIC have been limited to midrapidity. Measurements at forward rapidity are interesting for a variety of reasons. First is the need to constrain theoretical calculations over a wide kinematic range. The importance of this is demonstrated by the D0 measurement of bottom production at large rapidity ($\sqrt{s} = 1.8$ TeV, $p_T > 5$ GeV/c, $2.4 < y_\mu < 3.2$), as deduced from the production of high p_T muons [1]. Significant theoretical improvements resulted from the effort to reduce what was, initially, a discrepancy between theory and experiment that increased with increasing rapidity [5]. Second, significant cold nuclear effects have been seen in RHIC collisions at forward rapidity. PHENIX [47], BRAHMS [48,49], and STAR [50] have all measured light hadron production in $d + Au$ collisions at forward

rapidity and have found significant deviations from $R_{dAu} = 1$. It will be interesting to see whether charm production follows a similar pattern. Finally, open charm production at forward rapidity needs to be understood to fully interpret PHENIX J/ψ measurements at forward rapidity [24,25,51–53].

In this paper we report on the measurement of muon production at forward rapidity ($1.5 \leq |\eta| \leq 1.8$), in the range $1 < p_T < 3$ GeV/c, in $\sqrt{s} = 200$ GeV $p + p$ collisions by the PHENIX experiment. The upper limit of the p_T range is determined by available statistics. The vertex-independent muon yield is statistically extracted by calculating and subtracting contributions from light mesons (π's and K's) which decay into a muon, and hadrons which penetrate through the muon arm absorber material. In the absence of new physics, and in the p_T range measured in this analysis, such muons come dominantly from the decay of hadrons containing a charm quark (with small contributions from decays of hadrons containing a bottom quark and decays of light-vector mesons). PYTHIA is used to determine the charm quark spectrum that would produce the observed vertex-independent muon spectrum, and from this we obtain the differential cross section of charm quark production at forward rapidity. Although the statistical and systematic errors in this analysis preclude strong conclusions about the details of charm production, this paper establishes a method to extract this information from future PHENIX data sets.

The remainder of this paper is organized as follows: In Sec. II we describe the PHENIX experimental apparatus, with special emphasis on the muon arm detectors. In Sec. III we describe the methodology used to extract the vertex-independent muon signal. This section includes details on the run, event, and track selection criteria; values obtained for contributions to the muon yield from abundant light hadrons, which are subtracted to obtain the vertex-independent muon yield; and details on the systematic error analysis. In Sec. IV we extract the differential cross section for charm production at $y = 1.6$, integrated over p_T. Finally, in Sec. V we compare to other measurements, draw conclusions, and discuss the prospects for such measurements with improved data sets currently under analysis.

II. THE PHENIX EXPERIMENT

The PHENIX experiment [54], shown in Fig. 1, is a large multipurpose set of detectors optimized for measuring relatively rare electromagnetic probes (photons, muons, and electrons) of the spin structure of the proton and of the hot dense matter created in ultrarelativistic heavy ion collisions. The data acquisition system and multilevel triggers are designed to handle the very different challenges presented by $p + p$ collisions (relatively small events at very high rates) and $Au + Au$ collisions (very large events at relatively low rates) with little or no dead time [55,56].

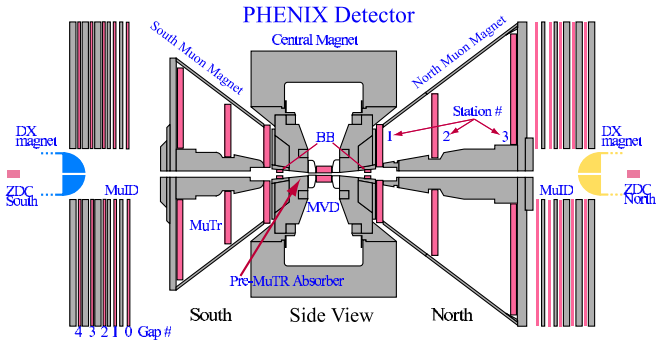

FIG. 1 (color online). Elevation view of the PHENIX experimental layout during the 2001/2 run period.

Event characterization devices, such as the beam-beam counters (BBCs) [57] used in this analysis, provide information on the vertex position, start time, and centrality of the collision. The two muon arms cover $1.2 < |\eta| < 2.4$ in pseudorapidity and $\delta\phi = 2\pi$ in azimuth. The two central arms, which each cover $|\eta| < 0.35$ and $\delta\phi = \pi/2$, are not used in this analysis.

The BBCs [57] each consist of 64 quartz radiators instrumented with mesh dynode photomultiplier tubes (PMTs) and arranged in a cylinder coaxial with the beam. The BBCs are placed on either side of the collision vertex and cover $3.0 < |\eta| < 3.9$. Each channel has a dynamic range extending to 30 times the average energy deposit of a minimum ionizing particle. The BBCs measure the arrival times of particles on both sides of the collision vertex, t_S and t_N. From the average of these times we determine the event start time. From their difference we obtain the position of the vertex along the beam direction, z_{vtx}. The BBCs also provide the minimum bias interaction trigger, which requires that there be at least one hit in each BBC and that $|z_{vtx}| < 38$ cm.

The muon arms [58] are coaxial with the beam on opposite sides of the collision vertex. By convention the arm on the south (north) end of the interaction region is assigned negative (positive) z coordinates and rapidity. For the 2001/2 run period, in which the data for this paper were collected, only the south muon arm was operational. Each muon arm is comprised of a muon tracker (MuTR) and a muon identifier (MuID). The MuTR makes an accurate measurement of particle momenta. The MuID allows coarse resolution track reconstruction through a significant amount of steel absorber. Together the muon arm detectors provide significant pion rejection (> 250:1, increasing with decreasing momentum) through a momentum/penetration-depth match.

Before ever reaching the MuTR detectors a particle must pass through the pre-MuTR absorber: 20 cm of copper (the nosecone) plus 60 cm of iron (part of the MuTR magnet). The nominal nuclear interaction lengths of iron and copper are $\lambda_I^{\mathrm{Fe}} = 16.7$ cm and $\lambda_I^{\mathrm{Cu}} = 15.3$ cm (although this varies with particle species and energy, see Sec. III F).

Therefore the pre-MuTR absorber presents a total thickness of $4.9\lambda_I/\cos\theta$, where θ is the polar angle of a particle's trajectory. This absorber greatly reduces the MuTR occupancy and provides the first level of pion rejection.

Each MuTR arm consists of three stations of cathode strip chambers installed in an eight-sided conical magnet [59]. The radial magnetic field ($\int \mathbf{B} \cdot \mathbf{dl} = 0.72$ T $\cdot$ m at 15 degrees, $B(\theta) \approx B(15°)\tan(\theta)/\tan(15°)$) bends particles in the azimuthal direction. Each station occupies a plane perpendicular to the beam axis and consists of multiple ionization gaps (3 gaps for the two stations closest to the collision vertex, 2 gaps for the last station) which have their charge imaged on two cathode strip planes oriented with a small stereo angle to provide two-dimensional information. An ionizing particle typically fires three adjacent strips in each orientation. A fit to the charge distribution on adjacent strips provides a position measurement with a resolution of $\sigma \approx 100$ μm in the bend direction. The MuTR achieves a momentum resolution of $\sigma_p/p \approx 5\%$, nearly independent of momentum over the analyzed kinematic range. The momentum independence is due to the significant contribution from energy-loss fluctuations in the pre-MuTR absorber, which falls as $1/p$, and which counters the more familiar linear momentum dependence seen for particles tracked through a ''thin'' detector.

Each MuID arm consists of five steel absorber plates interleaved with Iarocci tubes (operated in proportional mode) and specialized shielding to reduce backgrounds not originating from the collision vertex. Gaps are labeled 0–4 proceeding downstream from the collision point.

The Iarocci tubes, which are between 2.5 and 5 m in length, have eight 1 cm^2 square cells, each consisting of a three-sided ground electrode and an anode wire, mounted inside a polyvinyl chloride (PVC) gas enclosure. A readout channel (''two-pack'') is formed by wire-ORing the 16 anode wires of two tubes which are mounted in planes perpendicular to the beam axis and staggered by half of a cell width (0.5 cm). This provides redundancy, eliminates geometric inefficiency due to the cell walls, and reduces the maximum drift time for charge collection. Discriminator outputs from the two-pack signals provide a coarse one-dimensional hit position ($\sigma = 9$ cm$/\sqrt{12} = 2.6$ cm). The tubes in each gap are mounted in six individual panels, each of which contains two layers of two-packs (horizontally and vertically oriented), thus providing two-dimensional information.

The first MuID absorber plate (thickness = 20 cm—south; 30 cm—north) also serves as the return yoke of the MuTR magnet. Successive plates (identical for the two arms) are 10, 10, 20, and 20 cm thick, thus totaling $4.8\lambda_I/\cos\theta$ ($5.4\lambda_I/\cos\theta$) for the south (north) arm. Because of ionization energy loss a particle must have a momentum at the vertex which exceeds $2.31\cos\theta$ GeV$/c$ ($2.45\cos\theta$ GeV$/c$) to penetrate to the most downstream MuID gap of the south (north) arm.

Steel plates surrounding the beam pipe guard against backgrounds caused by low-angle beam-beam collision products which scrape the beam pipe near the MuID z-location (7–9 m) or shine off the RHIC dipole steering magnets immediately downstream of each MuID arm. Steel blocks in the RHIC tunnels guard against penetrating radiation generated by the incoming beams scraping against beamline components, primarily the final focusing quadrupole magnets.

The MuID also contributes information to the first-level trigger decision. For the 2001/2 run, during which the data for this analysis were collected, a relatively coarse trigger was implemented using memory lookup units (MLUs). Each gap was divided into quadrants with a horizontal and vertical split going through the beam axis. Signals from tubes in an individual gap/orientation (layer) and quadrant were logically combined. Only gaps 0, 2, 3, and 4 were used in the trigger due to the 16-bit input limitation of the MLUs. The penetration depth required for the trigger to fire was programmable. The *M1D* trigger fired if more than 6 out of 8 layers in a particular quadrant were hit (indicating the possibility that the event contained a particle penetrating to MuID gap 4). The *M1S* trigger fired if 3 of the 4 most shallow layers (horizontal and vertical layers in gaps 0 and 2) were hit for a particular quadrant. Both triggers required a coincidence with the BBC minimum bias trigger.

III. METHOD FOR EXTRACTION OF MUONS FROM CHARM DECAY

Inclusive muon candidates, N_I, are those particles which are successfully reconstructed to the last MuID gap (gap 4). These consist of four components:

(1) ''free-decay muons,'' N_D, which result from the decay of light hadrons (π and K mesons) before reaching the pre-MuTR absorber.
(2) ''punchthrough hadrons,'' N_P, which penetrate the entire detector and are thus misidentified as muons.
(3) ''background tracks,'' N_B, which in $p + p$ collisions are dominated by hadrons which decay into a muon after reaching the MuTR.
(4) ''vertex-independent muons,'' N_μ, which are primarily due to the decay of heavy flavor mesons.

Figure 2 shows a schematic depiction of the relative yield per event of these different contributions as a function of flightpath into the muon arms, as described below.

The number of hadrons is large and essentially independent of flightpath until the first absorber layer is reached. In each absorber layer these hadrons undergo strong interactions with a probability $\mathcal{P} \approx 1 - \exp(-L/\lambda)$, where L is the length of absorber material traversed, and λ is the species and p_T-dependent nuclear interaction length determined in Sec. III F. The punchthrough hadrons are that small fraction of hadrons ($< 0.4\%$) which penetrate to the last MuID gap and are indistinguishable from muons.

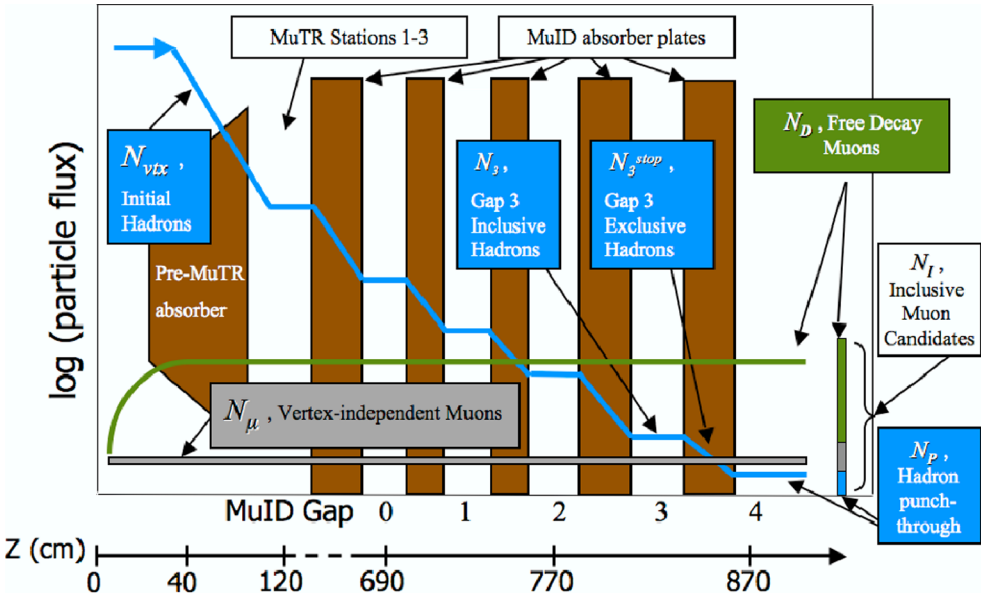

FIG. 2 (color online). Schematic depiction of the relative flux of different components of the inclusive muon candidate yield as a function of flightpath into the muon arm absorber (the nominal event vertex is at $z = 0$). See text for details.

The decay lengths for π's ($c\tau = 780$ cm) and K's ($c\tau = 371$ cm) are long compared to the flightpath from the vertex to the absorber. Therefore, the fraction of decay muons from these sources is relatively small, but increases linearly with the flightpath until the first absorber layer is reached. A hadron which decays prior to the pre-MuTR absorber into a muon that is inside the detector acceptance is indistinguishable from a muon originating at the vertex. After the first absorber layer the number of these free-decay muons remains constant by definition.

Hadrons which decay in the MuTR volume are a relatively small contribution for several reasons: most are absorbed prior to reaching the MuTR; the Lorentz-dilated decay lengths are long compared to the length of the MuTR volume (south ≈ 280 cm, north ≈ 420 cm); and a particle which decays in the MuTR is less likely to be reconstructed. Such tracks are partially accounted for in the calculation of punchthrough hadrons (see Sec. III F) and the remaining fraction falls under the category of background tracks (Sec. III G). This small contribution is not shown in Fig. 2.

Without a high-resolution vertex detector muons from various sources (the decay of open heavy flavor hadrons, the decay of quarkonia, the decay of light-vector mesons, and Drell-Yan production) originate indistinguishably close to the collision vertex. Thus their yield is independent of the flightpath and independent of the vertex position. Since inclusive muon candidates, by definition, penetrate to MuID gap 4, we measure the combined yield at $z \approx 870$ cm.

Figure 3 shows a sample distribution of the inclusive muon candidate yield as a function of collision vertex (z_{vtx}), and its decomposition into the four different contributions. The yield of free-decay muons is seen to have a linear dependence that is set to 0 at $z_{vtx} = z_{abs} - \lambda_D$. Here $z_{abs} = -40$ cm is the upstream face of the pre-MuTR absorber (indicated by the thick solid line), and λ_D is the effective absorption length, beyond which there are no free-decay muons. λ_D was found to be within a few mm of the species and p_T-dependent nuclear interaction lengths determined in Sec. III F. Muons originating from meson decays downstream of this location have no z_{vtx}

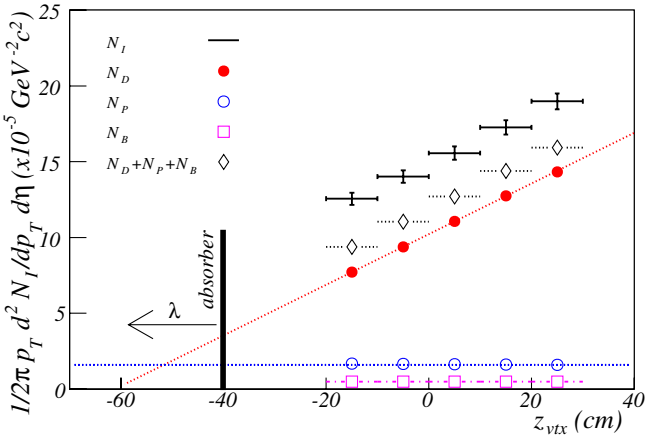

FIG. 3 (color online). Sample z_{vtx} distribution of different components of the inclusive muon candidate yield (measured data for both charge signs over the range $1.0 < p_T < 1.2$ GeV/c). Crosses show inclusive muon candidates, filled circles show free-decay muons, open circles show punchthrough hadrons, open squares show background tracks, and open diamonds show the sum of these three hadronic sources. The vertex-independent muon yield is obtained from the difference between the yield of inclusive muon candidates and the yield of light-hadronic sources.

dependence. The fraction not accounted for in the calculation of the punchthrough hadron yield forms the small contribution from background tracks. The yield of punchthrough hadrons and vertex-independent muons also have no z_{vtx} dependence. Note that the ratio of different contributions to the inclusive muon candidate spectrum is p_T dependent.

In order to extract the cross section for charm production we first need to determine the yield of vertex-independent muons, $N_\mu(p_T)$, the amount beyond that which is due to light hadrons and fake backgrounds. As described in Sec. III A, we select good runs, events, and tracks, and restrict our acceptance to regions where the detector was fully active, and the acceptance variation versus z_{vtx} was negligible. Next, as described in Secs. III B and III C, we obtain the yield of inclusive muon candidates vs p_T and z_{vtx}, corrected for acceptance and efficiency: $N_I(p_T, z_{vtx})$. In Sec. III D we describe a data-driven hadron generator. This generator is used in Sec. III E, in which we describe how the vertex dependence of the inclusive muon candidate yield allows us to obtain the yield of muons from light-meson decay before the pre-MuTR absorber, similarly corrected and binned: $N_D(p_T, z_{vtx})$. This generator is also used in Sec. III F, in which we describe how we use hadrons which stop in MuID gap 3 (the penultimate gap), together with simulations of hadron penetration in the MuID absorber, to obtain the yield of punchthrough hadrons in MuID gap 4: $N_P(p_T, z_{vtx})$. The yield of fake tracks, $N_B(p_T, z_{vtx})$, determined from simulations described in Sec. III G, is found to be small.

The yield of vertex-independent muons is determined by subtracting the contributions from light hadrons and fake backgrounds and averaging over z_{vtx} bins:

$$N_\mu(p_T) = \frac{1}{N_{z_{vtx}}} \sum_{j=1}^{N_{z_{vtx}}} N_I(p_T, z^j_{vtx}) - N_D(p_T, z^j_{vtx}) - N_P(p_T, z^j_{vtx}) - N_B(p_T, z^j_{vtx}), \quad (2)$$

where $d^2/2\pi p_T dp_T d\eta$ is implicit in all terms of the equation.

We convert this into a cross section via

$$\frac{d^2\sigma_\mu(p_T)}{2\pi p_T dp_T dy} = \frac{\sigma^{pp}_{BBC}}{\varepsilon^{c,\bar{c}\to\mu}_{BBC}} \frac{d^2N_\mu(p_T)}{2\pi p_T dp_T d\eta}. \quad (3)$$

Here σ^{pp}_{BBC} is the cross section of the BBC trigger for $p + p$ interactions and $\varepsilon^{c,\bar{c}\to\mu}_{BBC}$ is the efficiency of the BBC trigger for events in which a charm quark is created and decays into a muon. Substituting $\eta \to y$ introduces negligible error due to the small mass of the muon, the only component left after the subtraction. As described in Sec. III I, systematic errors are determined for each component and combined into a term that applies to the overall normalization and a term that applies to the p_T dependence of the spectrum.

We use PYTHIA to derive the p_T-dependent differential cross section for the production of charm quarks responsible for the vertex-independent muon yield. This procedure is very similar to that in Refs. [7–13], and is described in detail, along with the associated systematic error analysis, in Sec. IV.

A. Data reduction

1. Data sets and triggering

Runs were selected for this analysis based on stable detector operation using the same criteria as an earlier analysis of J/ψ production [51]. Further runs were eliminated due to the presence of large beam-related backgrounds entering the *back* of the detector.

We select only those events in the vertex range $-20 < z_{vtx} < 30$ cm. This minimizes the z_{vtx} dependence of the detector acceptance ($< 1\%$ over the entire z_{vtx} range, see Table II) and allows us to treat the amount of absorber material as a simple function of polar angle, ignoring complications in the pre-MuTR absorber near the beam pipe.

The decision to collect an event was made by the Local Level-1 Trigger [55] within 4μs of the collision. Input to the trigger decision was given by the BBC (collision with a valid event vertex) and the MuID (reconstructed penetrating track). Each trigger could be independently scaled down, so that it occupied a predetermined fraction of the available bandwidth, by selecting every N_i^{th} instance, where N_i is the scaledown factor for the i^{th} trigger. Three different data sets were selected from the good runs for different aspects of the data analysis:

(i) *BBC*: To extract N_D the z_{vtx} dependence of N_I is needed. The unbiased collision vertex distribution is obtained from a set of events collected with this trigger, which required at least one hit in each BBC counter and a vertex position, $|z_{vtx}| < 38$ cm. σ^{pp}_{BBC} was found to be 21.8 ± 2.1 mb using a van der Meer scan [60]. This uncertainty is included in the systematic error on the derived cross section, see Table VIII. There were 1.72×10^7 *BBC* triggered events passing offline vertex selection criteria in this data set ($-20 < z_{vtx} < 30$ cm), corresponding to a sampled luminosity of $\int Ldt = 0.79$ nb^{-1}.

(ii) *M1D*: In order to extract N_I, N_D, and N_B we used events selected with this trigger, which enriched the sample of events with tracks penetrating to MuID gap 4. For the *M1D* and *BBC* data sets we used identical run selection criteria. The total number of sampled *BBC* triggers for this data set was 5.77×10^8, corresponding to a sampled luminosity of $\int Ldt = 26.5$ nb^{-1}.

(iii) *M1S*: In order to extract N_P a data set which provides an unbiased measurement of the number of particles which penetrate to MuID gap 3 is needed. Since the *M1D* trigger required tracks to

penetrate to MuID gap 4 it could not be used. This trigger, which only used information from MuID gaps 0–2, is suitable. We used a subset of runs for which the scaledown factor for this trigger was only 10, corresponding to a sampled luminosity of $\int Ldt = 1.72\ \mathrm{nb}^{-1}$.

2. Track selection

The muon arm reconstruction algorithm starts by finding "roads" (collections of hits in the MuID which form straight, two-dimensional lines) and then combining them with hits in the MuTR to form "tracks." We apply strict cuts on both road and track parameters in order to reduce backgrounds, (see Table I).

The resulting purity of the selected tracks is demonstrated in Fig. 4. This figure shows $p\delta\theta$, the angular deviation through the pre-MuTR absorber, scaled by the particle momentum to give a quantity which should be momentum independent, for different p_T bins. As shown in Fig. 5, $\delta\theta$ is the angular difference between the reconstructed particle trajectory at the collision vertex ($x = 0$, $y = 0$, $z = z_{vtx}$) and at MuTR station 1. A GEANT [61] simulation of the PHENIX detector showed that tracks which do not suffer a strong interaction in the pre-MuTR absorber undergo angular deviations consistent with expectations based on standard multiple scattering: $\sigma_{\delta\theta} \propto \sqrt{x/X_0}/p$. The curves in each panel are fits to $Cp\delta\theta \exp(-(p\delta\theta)^2/2(p\sigma_{\delta\theta})^2)$, in which the normalization constant is allowed to float, and $p\sigma_{\delta\theta} = 130\ \mathrm{rad}\cdot\mathrm{MeV}/c$ is given by GEANT and is consistent with a simple estimate based on the radiation length of the pre-MuTR absorber and the standard multiple scattering formula [62–64] ($x/X_0 \approx 48 \rightarrow p\theta^{rms}_{\mathrm{space}} \approx (\sqrt{2}) \times (13.6\ \mathrm{MeV}/c)(\sqrt{48})\ \mathrm{rad} = 133\ \mathrm{rad}\cdot\mathrm{MeV}/c$). The integral beyond $3p\sigma_{\delta\theta}$ is $\approx 5\%$ and is largely due to hadrons which have a strong interaction in the pre-MuTR absorber and are still reconstructed as a muon candidate. Such tracks are accounted for in the calculation of the punchthrough hadron yield, as described below.

TABLE I. Road and track cuts. Here D_p is the penetration depth, defined to be the most downstream MuID gap with at least one hit (from the horizontal or vertical layer) associated with the track; z is the coordinate along the beam; x and y are transverse to each other and to the beam axis; the vertex cut refers to the transverse position of the MuID road projected to the xy plane at $z = 0$; and the slope cut refers to the direction cosine of the road in each transverse direction.

Road cuts:
· # Associated MuID hits >6 (out of a possible $2 \times D_p$)
· Vertex cut, $\sqrt{x^2 + y^2} < 100$ cm at $z = 0$
· Slope cut, $\sqrt{(\frac{dx}{dz})^2 + (\frac{dy}{dz})^2} > 0.25$
· ≥ 1 associated hit in MuID gap 4
Track cuts:
· Track fit quality, $\chi^2/\mathrm{dof} \leq 10$
· # Associated MuTR hits >12 (out of a possible 16)

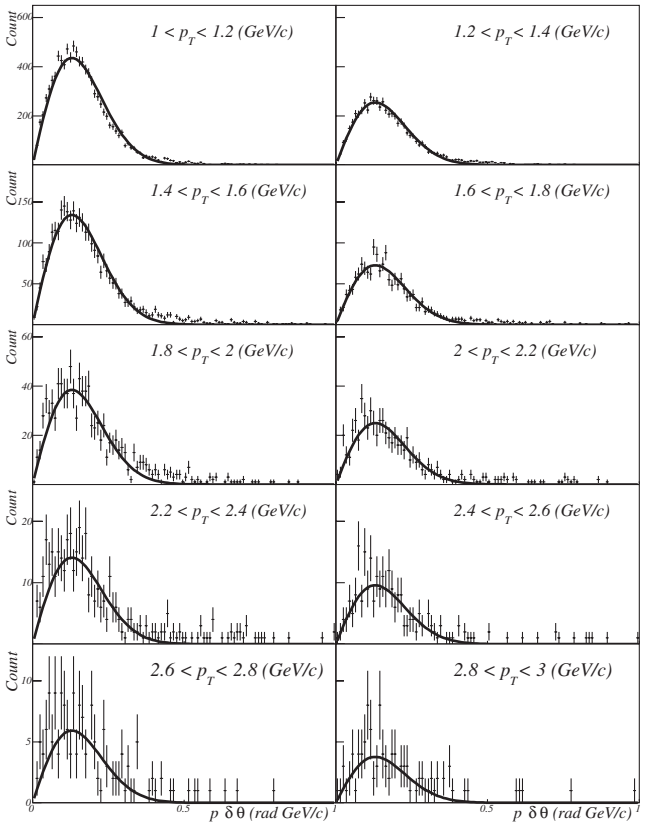

FIG. 4. The scaled angular deflection is the difference in a particle's polar angle caused by passage through the pre-MuTR absorber scaled by the particle's momentum, $p\delta\theta$. For muons (and hadrons not undergoing a strong interaction in the pre-MuTR absorber) one expects the distribution of this quantity to be well described by the standard multiple scattering formula. The different panels show $p\delta\theta$ for different p_T bins with fits (normalization only) to the expected distribution.

3. Acceptance restriction

We further restricted the acceptance of muon candidates for this analysis in two ways:

(1) Tracks were required to pass through regions of the detector that were fully active.
(2) Tracks were required to lie within a pseudorapidity range, $1.5 < |\eta| < 1.8$, in which the acceptance depends negligibly on the collision z_{vtx} location. As shown in Table II the variation is <1% over the entire z_{vtx} range.

B. Acceptance and efficiency

We evaluated four ratios to obtain the acceptance and efficiency for reconstructing tracks penetrating to a particular MuID gap, i:

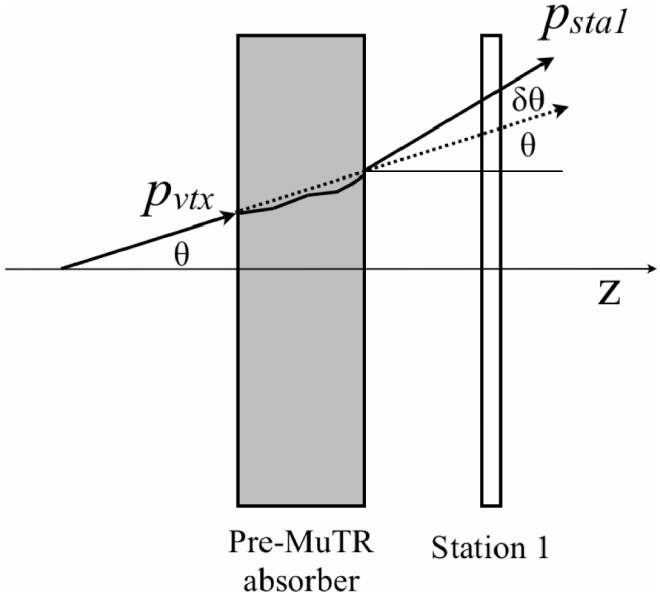

FIG. 5. The angular deflection $\delta\theta$ is the angular difference between the reconstructed particle trajectory at the collision vertex and at MuTR station 1. The momentum used to scale $\delta\theta$ is the average of the momentum reconstructed inside the MuTR magnet ($p_{\rm sta1}$) and the momentum extrapolated to the vertex (p_{vtx}).

(1) $\varepsilon^i_{\rm acc}$: the fraction of particles thrown in $2\pi\delta\eta$ ($\delta\eta = 0.3$) which penetrate to MuID gap 4, pass through active areas in every detector plane, and which pass the acceptance restrictions described above. This quantity ($\approx 50\%$) accounts for nonsensitive structural members in between the cathode strip chambers and chamber regions removed from consideration for the entirety of this analysis.

(2) $\varepsilon^i_{\rm rec}$: the fraction of particles within the accepted region, defined in the previous step, that are reconstructed. This quantity is somewhat low (64%) due to detector problems in this first physics run that have been subsequently resolved.

(3) $\varepsilon^i_{\rm user}$: the fraction of reconstructed tracks that pass the cuts listed in Table I.

(4) $\varepsilon^i_{\rm trig}$: the fraction of selected tracks that fire the MuID trigger.

The overall acceptance and efficiency is the product of these ratios. Note that by construction these ratios factorize since the denominator of each successive ratio is the numerator of the previous ratio.

$\varepsilon^i_{\rm acc}$, $\varepsilon^i_{\rm rec}$, and $\varepsilon^i_{\rm user}$ were evaluated with a GEANT simulation using single muons thrown with a realistic p_T spectrum into the muon arms. The applied detector response incorporated measured detector performance. Reductions in efficiency due to occupancy are negligible in $p + p$ collisions. Run-to-run variations were ignored since we selected runs in which the detector performance was similar and stable. For cuts used in this analysis the acceptance and efficiency are the same for different components of the inclusive muon candidate yield. Efficiency values for tracks penetrating to MuID gap 4 were parametrized in terms of z_{vtx} and p_T and are listed in Table II. There are minor differences in these parametrizations for particles with different charge sign. Fit errors on these parametrizations are included in the systematic uncertainty, as shown in Table V.

We also determined the efficiencies for tracks which only penetrate to MuID gap 3, since these are needed to obtain the yield of punchthrough hadrons. These were found to scale from the efficiencies for tracks penetrating to MuID gap 4: $\varepsilon^3_{\rm acc}\varepsilon^3_{\rm rec}\varepsilon^3_{\rm user} = \varepsilon^3_{\rm scale} \times \varepsilon^4_{\rm acc}\varepsilon^4_{\rm rec}\varepsilon^4_{\rm user}$, where $\varepsilon^3_{\rm scale} = 0.66$. $\varepsilon^3_{\rm scale}$ is less than one because the MuID and the road reconstruction algorithm are optimized for deeply penetrating particles. Particles which do not penetrate to the last gap have poorer resolution matching to MuTR tracks (due to reduced lever arm and smaller number of hits) and are also more susceptible to MuID inefficiencies. There is considerable ambiguity in determining which particles *should* have been reconstructed. Different definitions, together with statistical uncertainties, combined to give a systematic error of 23%, as shown in Table VII.

Trigger efficiencies, $\varepsilon^3_{\rm trig}$ and $\varepsilon^4_{\rm trig}$, are also listed in Table II. These were evaluated using the *BBC* data set, which did not require the MuID trigger to fire.

$$\varepsilon^4_{\rm trig} = \frac{(N_4|M1D) \times S_{M1D}}{(N_4|BBC) \times S_{BBC}}, \tag{4}$$

where $N_4|M1D$ is the number of selected tracks penetrating to MuID gap 4 for events in which the *M1D* trigger fired, S_{M1D} is the scaledown factor applied to the *M1D* trigger, and similarly for $M1D \rightarrow BBC$. $\varepsilon^3_{\rm trig}$ was also evaluated according to Eq. (4), but with $N_4 \rightarrow N_3$, and $M1D \rightarrow M1S$. Different procedures for calculating $\varepsilon^3_{\rm trig}$ gave slightly different answers, resulting in the assignment of a 4.7% systematic error, as shown in Table V.

TABLE II. Trigger, acceptance, track reconstruction, and track selection efficiencies. In the formulae below, the units for p_T are GeV/c and the units for z_{vtx} are cm. Systematic errors for these quantities are given in Tables V and VII.

Quantity	Value
$\varepsilon^{4,+}_{\rm acc}$	$0.51 \times (1 - 114\exp(-5.9p_T)) \times (1 + 0.0015z_{vtx})$
$\varepsilon^{4,-}_{\rm acc}$	$0.50 \times (1 - 531\exp(-7.5p_T)) \times (1 + 0.0013z_{vtx})$
$\varepsilon^{4}_{\rm rec}$	0.64
$\varepsilon^{4,+}_{\rm user}$	$0.74 \times (1 - 0.0019z_{vtx})$
$\varepsilon^{4,-}_{\rm user}$	$0.74 \times (1 - 0.0009z_{vtx})$
$\varepsilon^{3}_{\rm scale}$	0.66
$\varepsilon^{4}_{\rm trig}$	0.86
$\varepsilon^{3}_{\rm trig}$	0.97
$\varepsilon^{c,\bar{c}\rightarrow\mu}_{\rm BBC}$	0.75

Since both the *M1D* and *M1S* triggers required a coincidence with the *BBC* trigger we must also account for the *BBC* trigger efficiency for events in which a reconstructed muon is created via charm quark decay: $\varepsilon_{BBC}^{c,\bar{c}\to\mu}$. The BBC efficiency was evaluated for events in which a J/ψ was produced in the muon arm acceptance using PYTHIA + GEANT simulations [51]. The BBC efficiency was also evaluated for events in which π^0's were produced in the central arm acceptance [60] using data triggered without a BBC requirement. The BBC efficiency under both conditions was found to have a similar value that we therefore adopt: $\varepsilon_{BBC}^{c,\bar{c}\to\mu} = 0.75 \pm 0.04$. This uncertainty is included in the systematic error on the derived cross section (Table VIII).

C. Inclusive muon candidates

We first form two sets of collision vertex (z_{vtx}) histograms with 10 cm bins: one histogram for all interactions selected with the *BBC* trigger, and a series of histograms for interactions selected with the *M1D* trigger and having a good muon candidate within a p_T bin ($1 < p_T < 3$ GeV/c, 200 MeV/c bins). The muon candidate histograms are formed separately for each charge sign. Entries into each histogram are scaled by the appropriate trigger scaledown factor. The muon candidate histograms are divided by the minimum bias histogram to give $N_I(p_T, z_{vtx})$, as shown in Fig. 6. Systematic errors shown in this figure are discussed in Sec. III I and listed in Table V.

In Fig. 6 one can clearly see the linear dependence in the yield of inclusive muon candidates vs z_{vtx} at low transverse momentum ($p_T < 2$ GeV/c). This dependence is due to muons from the decay of abundant light hadrons (π's and K's) prior to the pre-MuTR absorber material at $z_{abs} = -40$ cm. One also observes a charge asymmetry, with the yield of positives significantly exceeding that of negatives. This is due to the substantial charge asymmetry in the kaon nuclear interaction length—positive kaons are much more likely to punch through the muon arm absorber than any other species. This effect is discussed in Sec. III F.

D. Hadron generator

The background components of the inclusive muon candidate yield (free-decay muons (Sec. III E), and punch-through hadrons (Sec. III F)) arise from charged hadrons,

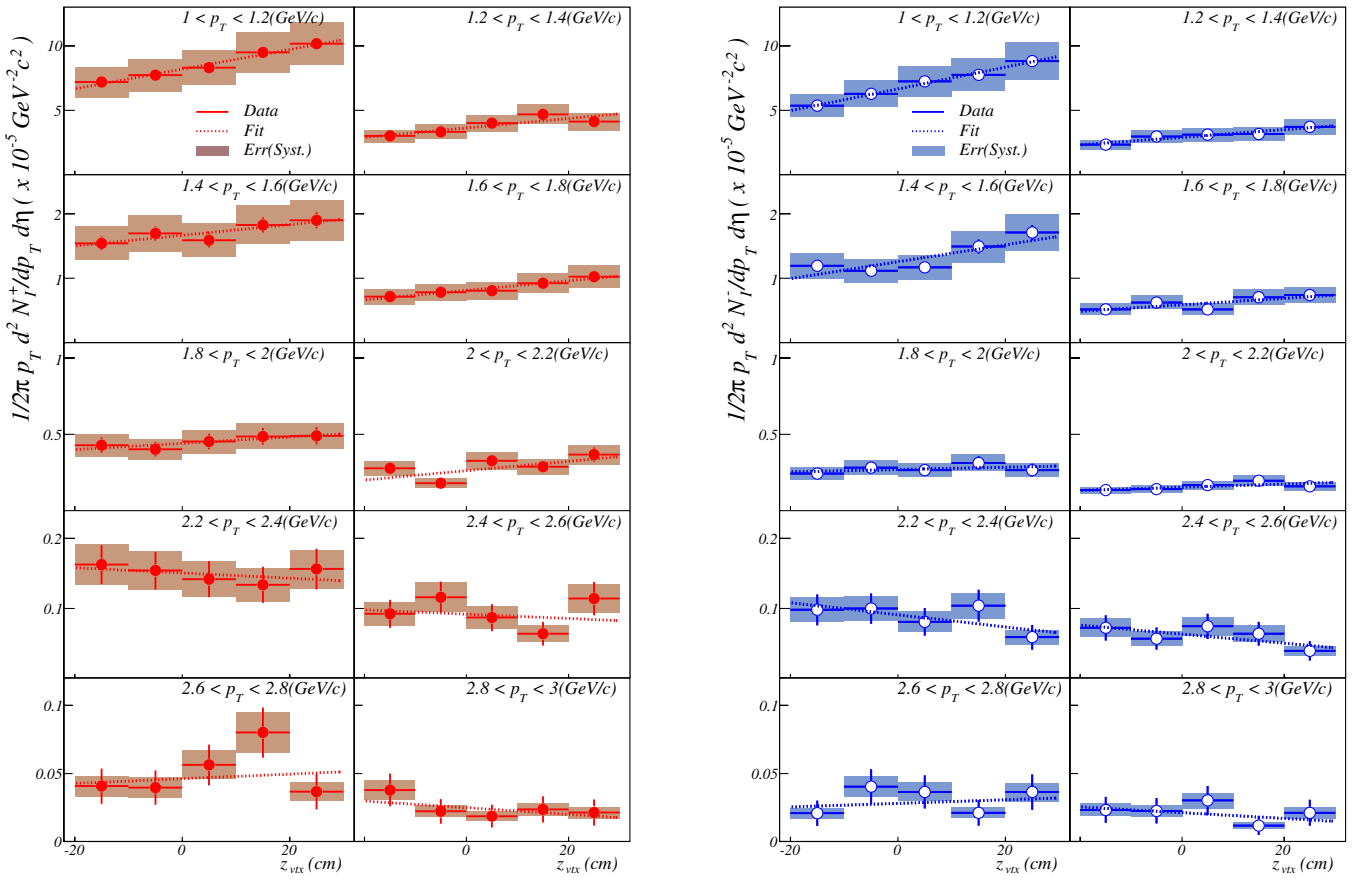

FIG. 6 (color online). Yield of (left) positively and (right) negatively charged inclusive muon candidates vs z_{vtx} for different p_T bins. Fits shown use the functional form $a + bz_{vtx}$ to extract the contribution from hadron decay, as discussed in Sec. III E. Error bars show statistical errors. Shaded bands show systematic errors, as discussed in Sec. III I and listed in Table V. The substantial charge asymmetry is due to the relatively long nuclear interaction length for positive kaons, as discussed in Sec. III F.

primarily pions and kaons, produced in the kinematic range of our measurement. There are no measurements of hadron production in this kinematic range and model predictions have substantial disagreement. This disagreement would lead to unacceptable systematic uncertainty in the extraction of the heavy flavor muon component. In order to reduce this uncertainty we developed a data-driven hadron generator that is based on PHENIX midrapidity measurements and then constrained by the z_{vtx} dependence of the inclusive muon candidate yield presented in this analysis.

The input for this generator is obtained from PHENIX measurements in $\sqrt{s} = 200$ GeV $p + p$ collisions at $y = 0$ [65,66] using the following procedure:

(1) π^+ and π^- spectra at $y = 0$ ($0 < p_T < 3.5$ GeV/c) are fit to a power law and then scaled assuming a Gaussian rapidity dependence ($\sigma_y = 2.5$) and $y - p_T$ factorization:

$$N^{\pi^\pm}_{y=1.65}(p_T) = N^{\pi^\pm}_{y=0}(p_T)\exp(-(1.65^2/2\sigma_y^2)).$$

This rapidity dependence and factorization is observed both in PYTHIA and in BRAHMS [49] data measured at $y = 1$ and $y = 2.2$.

(2) A similar procedure is used to obtain the charged kaon yield at $y = 1.65$.
First the charged kaon yield at $y = 0$ is extrapolated beyond the current measurement limit ($p_T < 2$ GeV/c). To do this we form the isospin averaged K/π ratio vs p_T at $y = 0$. We use charged particles, $(K^+ + K^-)/(\pi^+ + \pi^-)$, for $p_T < 2$ GeV/c [65] and neutral particles, K^0/π^0, for $2 < p_T < 6.5$ GeV/c [66]. This combined ratio is then fit to $f(p_T) = A(1 - B\exp(-Cp_T))$. This function is then normalized separately to the K^+/π^+ and K^-/π^- ratios for $p_T < 2$ GeV/c and multiplied by the corresponding charged pion spectrum to obtain $N^{K^\pm}_{y=0}(p_T)$, our parametrization of the midrapidity charged kaon p_T spectra extending out to 3.5 GeV/c.
As with pions, we need to extrapolate this parametrization of the yield at $y = 0$ to obtain the yield at $y = 1.65$. One possibility is to assume boost invariance of the K/π ratio. However, PYTHIA gives a slightly narrower rapidity distribution for kaons than for pions, resulting in a kaon yield at $y = 1.65$ that is only 85% of that predicted with the boost invariance assumption. We split the difference between these two assumptions:

$$N^{K^\pm}_{y=1.65}(p_T) = 92.5\% N^{K^\pm}_{y=0}(p_T) \times \exp(-(1.65^2/2\sigma_y^2)),$$

where, again, $\sigma_y = 2.5$.

(3) The p and $\bar{p}$ spectra are assumed to have the same shape as the pion spectra with normalization factors set to the measured values at $y = 0$, $p_T = 3$ GeV/c (0.4 for p/π^+, 0.24 for $\bar{p}/\pi^-$) [65]. The exact form used for the p, $\bar{p}$ spectra is unimportant. They obviously do not contribute to the yield of decay muons and their contribution to the yield of punchthrough hadrons is greatly suppressed due to their relatively short nuclear interaction length.

E. Free-decay muons

We fit the histograms shown in Fig. 6 with the function $a + bz_{vtx}$. After multiplying by $dz/dl_{fp} = \cos(\langle\theta\rangle) = 0.947$ the slope, b, and its fit error give, respectively, the yield *per unit length of decay flightpath* of muons from hadron decay, $dN_D(p_T)/dl_{fp}$, and the statistical error on this quantity. We do not allow a to vary in the fit, but we perform the fits for different values of a to account for uncertainty in that quantity. We also allow the z_{vtx} fit range to vary from $|z_{vtx}| < 20$ cm to $|z_{vtx}| < 40$ cm. The resulting variations in N_D (5% and 3.3%, respectively) are incorporated into the systematic error, as shown in Table VI. Results are shown in Fig. 7.

This procedure does not provide a quantitative measure of the decay muon spectrum above $p_T \sim 2$ GeV/c, even though a substantial fraction of the inclusive muons are decay muons up to significantly higher p_T. This is due to the fact that at high p_T the decay slopes decrease (Lorentz time dilation) as do the statistics, both of which make it more difficult to quantify the decay component directly.

In order to extend our estimate of decay muons to higher p_T we simulate charged hadron spectra using the hadron generator described in Sec. III D. These hadrons are allowed to decay into the muon arms, resulting in a predicted p_T spectra (per unit length) of muons from hadron decay separately for each charge sign. We then normalize these predicted spectra to the measured spectra. The normalized predicted spectra are shown as the dashed lines in Fig. 7. The predicted spectral shape agrees with the data where we have a statistically significant measurement. The absolute normalization of the prediction is within 7% of the measured value, easily consistent within errors. This difference, and the effects of reasonable variations on the input spectral shapes, are incorporated into the systematic uncertainty on N_D, as listed in Table VI.

We obtain $N_D(p_T, z_{vtx})$ from the product of $dN_D(p_T)/dl_{fp}$ and the average value of the decay flightpath, $l_{fp} = \lambda_D + |z_{vtx} - z_{abs}|/\cos(\theta)$, for each z_{vtx} bin.

F. Punchthrough hadrons

A reconstructed hadron that penetrates to MuID gap 4 is impossible to distinguish from a muon. The straightforward technique to calculate the contribution of this background component would be to use the PHENIX GEANT-based Monte Carlo program to simulate the response to hadrons sampled from the hadron generator spectra. However, this approach suffers from unacceptable systematic uncertainty due to differences in the predictions for

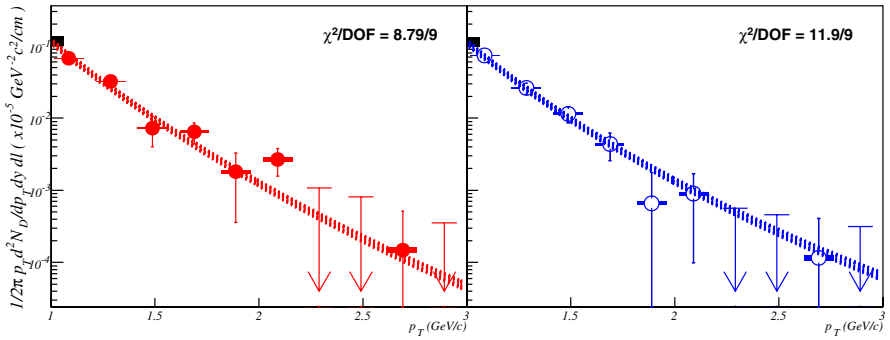

FIG. 7 (color online). Yield per unit length of (left) positively and (right) negatively charged free-decay muons. Points are the measured values determined by linear fits to the inclusive muon candidate yield (Fig. 6). Error bars indicate statistical errors for those fits. p_T bins with a negative (nonphysical) slope in those fits are shown with a line at the 90% C.L. upper limit (statistical errors only) and an arrow pointing down. See Sec. III E for details. Dashed lines are the predictions for each sign from the data-driven hadron generator with the normalization fit to the measured points. See Sec. III D for details. The χ^2/dof for these fits are indicated. The width of the lines corresponds to σ_{R_D} (Table VI), the error on the ratio of free-decay muons to inclusive muon candidates. Black bands at the left edge of each panel show the p_T-independent systematic error on the inclusive muon candidate yield. Shaded bands on each point show the systematic errors that affect the p_T shape of the inclusive muon candidate spectrum. These last two systematic errors (Table V) need to be included in the total error budget for the yield of free-decay muons, σ_{N_D}/N_D (Table VI), but are displayed separately since they are common to all components of the inclusive muon candidate yield. See Eqs. (12) and (13). Systematic errors are discussed in Sec. III I.

different hadronic interaction packages implemented in GEANT. To avoid this limitation we developed a procedure in which we cleanly identify hadrons in shallow gaps and then extrapolate their yield to obtain the yield of punchthrough hadrons in MuID gap 4.

Figure 8 shows the longitudinal momentum (p_z, the momentum projected onto the beam axis) distribution of particles that *stop* in MuID gap 3. The sharp peak at $p_z \approx 2.2$ GeV/c corresponds to charged particles which stopped because they ranged out in the absorber plate between gaps 3 and 4 (this includes both muons and also hadrons which only suffered ionization energy loss.) The width of this peak is due to the 20 cm (11.4 X_0) absorber thickness between MuID gaps 3 and 4, and energy-loss fluctuations in all the preceding absorber layers. Particles at momenta beyond the peak ($p_z > 3$ GeV/c) form a relatively pure sample of hadrons, with only a negligible contamination due to inefficiencies in MuID gap 4 and particles with misreconstructed momentum values. After correcting for acceptance and efficiency these particles are used to obtain the p_T spectrum for the "gap 3 exclusive yield," as shown in Fig. 9. We use data from the *M1S* trigger sample since the *M1D* sample required a hit in MuID gap 4, which would bias this measurement.

In order to extrapolate this measured spectrum for hadrons stopping in MuID gap 3 to the spectrum of punchthrough hadrons which penetrate to MuID gap 4, we start by assuming exponential absorption of hadrons entering the muon arm absorber material. With this assumption we obtain an expression for the "gap 3 inclusive yield," those hadrons that reach *at least* MuID gap 3:

$$N_3^i(p_T, \theta) = N_{vtx}^i(p_T, \theta) \exp(-L_3(\theta)/\lambda^i(p_T)), \quad (5)$$

where i indicates the contributing hadron species ($\pi^{\pm}$, $K^{\pm}$, p, $\bar{p}$), $N_{vtx}^i(p_T, \theta)$ is the yield at the vertex of the i^{th} species, $L_3(\theta)$ is the amount of absorber material traversed to reach MuID gap 3, and $\lambda^i(p_T, \theta)$ is the p_T-dependent nuclear interaction length of the i^{th} species. We can write a similar expression for the punchthrough hadron yield:

$$N_P^i(p_T, \theta) = N_{vtx}^i(p_T, \theta) \exp(-L_4(\theta)/\lambda^i(p_T)), \quad (6)$$

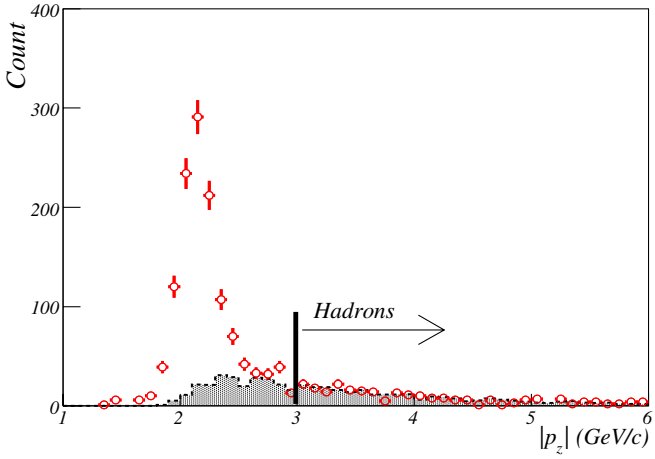

FIG. 8 (color online). Points (measured data) show the longitudinal momentum, measured at the vertex (p_z^{vtx}), of particles that stop in MuID gap 3. The sharp peak is due to muons which range out in the absorber plate between gaps 3 and 4. The histogram (Monte Carlo) shows the longitudinal momentum of all particles that stop in MuID gap 3 and do not decay before the pre-MuTR absorber. The Monte Carlo is normalized to the data for $p_z^{vtx} > 3$ GeV/c. Particles beyond the peak form a relatively pure sample of hadrons.

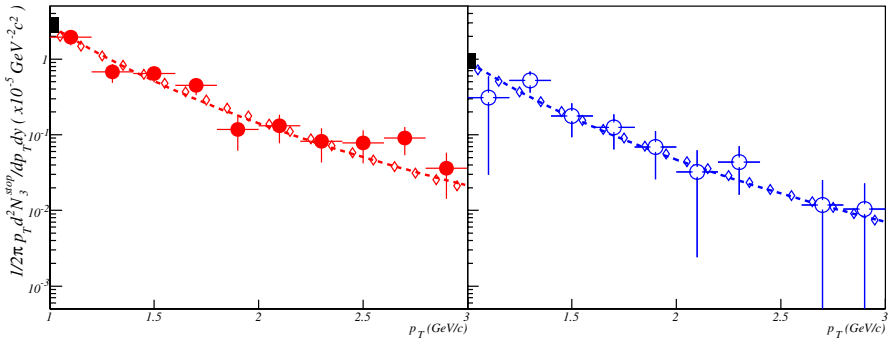

FIG. 9 (color online). Points show the p_T spectrum of (left) positively and (right) negatively charged hadrons stopping in MuID gap 3 (''gap 3 exclusive yield'') with statistical errors. Open diamonds show a power-law fit to the data, effectively a smoothed version of the data. Dashed lines are fits to the smoothed data using the hadron generator (normalized by the measured free-decay spectrum, as shown in Fig. 7) and Eqs. (8) and (9) to obtain values for the species-dependent nuclear interaction lengths, $\lambda^i(p_T)$.

where $L_4(\theta)$ is the amount of absorber material traversed to reach MuID gap 4.

By taking the difference between these two equations we obtain an expression for the gap 3 exclusive yield:

$$\begin{aligned} N_3^{i,\mathrm{stop}}(p_T,\theta) &= N_3^i(p_T,\theta) - N_P^i(p_T,\theta) \\ &= N_{vtx}^i(p_T,\theta)\exp(-L_3(\theta)/\lambda^i(p_T)) \\ &\quad\times(1-\exp((L_3(\theta)-L_4(\theta))/\lambda^i(p_T))). \end{aligned} \quad (7)$$

The species comprising the gap 3 exclusive yield are not determined, but their charge sign is. As a result, Eq. (7) can be rewritten as two equations with six unknowns for each p_T bin:

$$\begin{aligned} N_3^{+,\mathrm{stop}}(p_T,\theta) &= N_3^+(p_T,\theta) - N_P^+(p_T,\theta) \\ &= \sum_{i=\pi^+,K^+,p} N_{vtx}^i(p_T,\theta)\exp(-L_3(\theta)/\lambda^i(p_T)) \\ &\quad\times(1-\exp((L_3(\theta)-L_4(\theta))/\lambda^i(p_T))), \end{aligned} \quad (8)$$

$$\begin{aligned} N_3^{-,\mathrm{stop}}(p_T,\theta) &= N_3^-(p_T,\theta) - N_P^-(p_T,\theta) \\ &= \sum_{i=\pi^-,K^-,\bar{p}} N_{vtx}^i(p_T,\theta)\exp(-L_3(\theta)/\lambda^i(p_T)) \\ &\quad\times(1-\exp((L_3(\theta)-L_4(\theta))/\lambda^i(p_T))). \end{aligned} \quad (9)$$

Based on measured cross sections for various species [67], the number of unknowns is reduced with the following assumption:

$$\begin{aligned} \lambda^{K^+} &= \lambda^{\mathrm{long}}, \\ \lambda^p = \lambda^{\pi^+} = \lambda^{\pi^-} = \lambda^{K^-} &= \lambda^{\mathrm{short}}, \\ \lambda^{\bar{p}} &= 0. \end{aligned}$$

We further assume that λ^{short} and λ^{long} have the form $a + b(p_T[\mathrm{GeV}/c] - 1)$.

We effectively smoothed the gap 3 exclusive yield for each sign by fitting the measured values to a power law. Using $N_{vtx}^i(p_T,\theta)$ from the hadron generator (normalized to the free-decay muon spectrum, as described in Sec. III E) and known values for $L_{3,4}(\theta)$, we fit Eqs. (8) and (9) to the smoothed gap 3 exclusive yield for each sign to obtain:

$$\lambda^{\mathrm{short}} = 19.0 + 2.2(p_T[\mathrm{GeV}/c] - 1)\ \mathrm{cm}, \quad \text{and}$$
$$\lambda^{\mathrm{long}} = 25.9 + 4.4(p_T[\mathrm{GeV}/c] - 1)\ \mathrm{cm}.$$

Results of these fits are shown in Fig. 9. The fit error on the normalization (10%) is incorporated into the systematic error, as listed in Table VII.

With these values for $\lambda^i(p_T)$ and the hadron generator input spectra, we could directly apply Eq. (6) to obtain the final punchthrough spectra. However, we made one further correction, described below, after finding that our assumption of exponential absorption does not hold when applied to GEANT simulations of the punchthrough process.

Using our GEANT-based PHENIX simulation program, we generated data sets with both the FLUKA [68] and GHEISHA [69] hadronic interaction packages. Input spectra for these data sets were given by our decay hadron generator. We selected all particles which did not decay before the pre-MuTR absorber. ''Truth'' values for the punchthrough and gap 3 exclusive yields were obtained by splitting those particles based on the absence (gap 3 exclusive) or presence (punchthrough) of associated charged particles with $E_4 > 100$ MeV in MuID gap 4. We varied E_4 from 50–300 MeV and saw no significant change in the results.

Using the known input spectra, known values for $L_{3,4}(\theta)$, and truth values for the gap 3 exclusive yield, we applied Eq. (7) to the Monte Carlo data sets to obtain $\lambda^i(p_T)$. Because of statistical limitations we integrated our results over θ and into two p_T bins: $1 < p_T < 2$ GeV/c and $p_T > 2$ GeV/c. Values extracted for $\lambda^i(p_T)$ for the different hadronic interaction packages are listed in Table III.

TABLE III. Nuclear interaction lengths, $\lambda^i(p_T)$, for different particle species and p_T bins (in GeV/c) for FLUKA and GHEISHA. Statistical errors on these values are ≈ 2 mm.

	FLUKA $\lambda^i(p_T)$ [cm]		GHEISHA $\lambda^i(p_T)$ [cm]	
Species	$1 < p_T < 2$	$p_T > 2$	$1 < p_T < 2$	$p_T > 2$
π^+	19.6	24.5	16.0	21.1
π^-	19.4	24.8	15.0	19.3
K^+	24.4	29.6	24.9	30.8
K^-	20.5	24.2	17.2	21.2

These values are consistent with those found for our measured data, listed above.

Inserting these values for $\lambda^i(p_T)$ into Eq. (6) we obtained a prediction for $N_P^i(p_T, \theta)$. Ratios of the truth values and predicted values for the punchthrough yield ($R_{N_P^i(p_T)}$) for the different hadronic interaction packages are listed in Table IV. The limitation of the simple exponential absorption model is illustrated by the fact that these ratios deviate significantly from unity. Furthermore, the two hadronic interaction packages disagree on the direction of the deviation: the exponential absorption model tends to overpredict the punchthrough yield for FLUKA and underpredict it for GHEISHA.

TABLE IV. Ratios, $R_{N_P^i(p_T)}$, of truth values for the punchthrough hadron yield to those predicted assuming exponential hadron absorption for different particle species and p_T bins (in GeV/c), for FLUKA and GHEISHA. Average values of the ratios for the two different hadronic interaction packages, $\langle R\rangle^i \times (p_T)$, are smoothed across the p_T bin at 2 GeV/c to obtain correction factors for the exponential absorption model. Statistical errors on these quantities are $\approx 10\%$. The maximum fractional difference in the ratios for the two different packages (32%) is incorporated into the systematic error estimate, as shown in Table VII.

Species	$1 < p_T < 2$	$p_T > 2$	Description
π^+	0.76	0.86	$R^{\mathrm{FLUKA}}_{N_P^i(p_T)}$
π^-	0.91	0.75	
K^+	0.91	1.00	
K^-	1.17	1.06	
π^+	1.48	1.04	$R^{\mathrm{GHEISHA}}_{N_P^i(p_T)}$
π^-	1.47	1.09	
K^+	1.31	1.07	
K^-	2.21	1.69	
π^+	1.12	0.95	$\langle R\rangle^i(p_T)$
π^-	1.19	0.92	
K^+	1.11	1.04	
K^-	1.67	1.38	
π^+	32%	10%	$\delta R_{N_P^i(p_T)}/C^i(p_T)$
π^-	24%	18%	
K^+	18%	3%	
K^-	32%	22%	

Relatively little data exist in the relevant momentum range that would allow us to conclude which, if either, hadronic interaction package is correct. Measurements by RD10 and RD45 [70] of the penetration depth of identified hadrons found that GHEISHA did well for protons and FLUKA did not. But neither did well for pions and no data exist for kaons. Furthermore, the results are sensitive to the definition of a penetrating particle. For RD10/45 an incoming particle with any associated charged particles in the 120×120 cm^2 detector area at a particular depth was defined to have penetrated to that depth. In our measurement we reconstruct particle trajectories, and MuID hits are not associated with a road unless they are within a narrow search window surrounding the projected trajectory. Thus we are relatively insensitive to the leakage of a showering hadron.

As a result of these uncertainties on the applicability of our exponential absorption model we incorporate a species and p_T-dependent correction factor to Eq. (6):

$$N_P^i(p_T, \theta) = C^i(p_T) N_{vtx}^i(p_T, \theta) \exp(-L_4(\theta)/\lambda^i(p_T)). \tag{10}$$

The correction factors for pions and kaons are obtained from the average of the values of $R_{N_P^i(p_T)}$ for the two packages, $\langle R\rangle^i(p_T) = (R^{\mathrm{FLUKA}}_{N_P^i(p_T)} + R^{\mathrm{GHEISHA}}_{N_P^i(p_T)})/2$, which are listed in Table IV. We incorporate the maximum fractional difference in the ratios for the two packages (32%) into our systematic error estimate, as listed in Table VII. The values of $\langle R\rangle^i(p_T)$ for a given species are not the same for the different p_T bins. Therefore we assume the values are valid at the average p_T of each bin ($p_T = 1.25$ GeV/c and 2.31 GeV/c, respectively) and use a linear extrapolation in p_T to obtain the final correction factors:

$$C^i(p_T) = \langle R\rangle^i_{\mathrm{low}\ p_t} + (\langle R\rangle^i_{\mathrm{high}\ p_t} - \langle R\rangle^i_{\mathrm{low}\ p_t}) \times \frac{p_T[\mathrm{GeV}/c] - 1.25}{2.31 - 1.25}. \tag{11}$$

We assume that p's and $\bar{p}$'s have the same correction factors as the corresponding sign pions. Since p's and $\bar{p}$'s make only small contributions to the punchthrough hadrons this simplifying assumption has little consequence. We incorporate a conservative 10% systematic error on N_P to cover extreme possibilities for the p and $\bar{p}$ nuclear interaction lengths, as shown in Table VII.

We use Eq. (10), with the tabulated correction factors, particle yields at the vertex given by our normalized hadron generator, the known value of $L_4(\theta)$, and the values for $\lambda^i(p_T)$ determined from the measured gap 3 exclusive yield, to obtain the p_T spectrum of punchthrough hadrons, $N_P(p_T)$, as shown in Fig. 10. Systematic errors shown in this figure are discussed in Sec. III I and listed in Table VII. We multiply $N_P(p_T)$ by the fraction of the accepted z_{vtx}

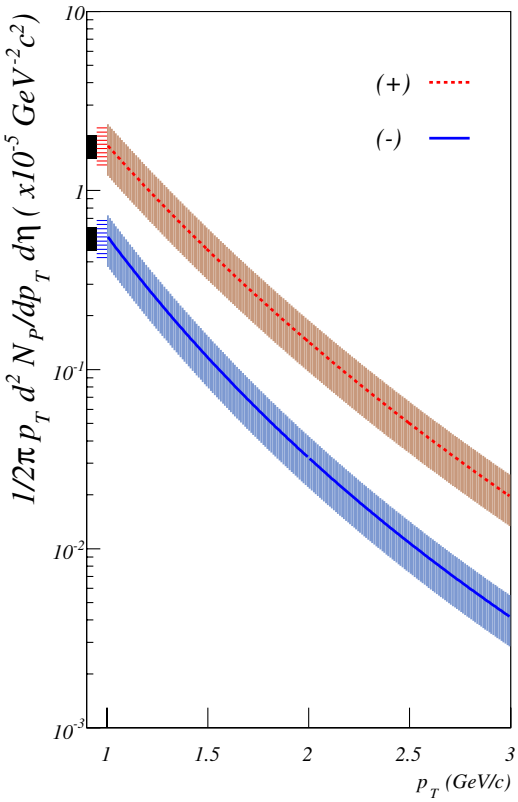

FIG. 10 (color online). Yield of positively (dotted line) and negatively (solid line) charged hadrons which penetrate to MuID gap 4. The curves are obtained from Eq. (10), as described above. Solid bands on the y-axis show the relative normalization uncertainty on the inclusive muon candidate yield, $\sigma^{\mathrm{norm}}_{N_I}/N_I$ (Table V). This needs to be included in the total error budget for the yield of punchthrough hadrons, σ_{N_P}/N_P (Table VII), but is displayed separately since it is common to all components of the inclusive muon candidate yield (see Eqs. (12) and (13)). Hatched bands on the y-axis show $\sigma^{\mathrm{norm}}_{R_P}$ (Table VII), the normalization uncertainty on the ratio of punchthrough hadrons to inclusive muon candidates. The relative fraction of positive and negative punch through hadrons can move up and down together by this amount. Shaded bands around the extracted punchthrough hadron yield show the systematic errors on $\sigma^{p_T}_{R_P}$ which can affect the p_T shape of the relative fraction of positive and negative punch through hadrons (positives and negatives can move independently). These are dominated by differences in the applicability of the simple exponential absorption model observed for FLUKA and GHEISHA. Systematic errors are listed in Tables V and VII and discussed in Sec. III I.

range represented by each z_{vtx} bin to finally obtain $N_P(p_T, z_{vtx})$.

The charge asymmetry in Fig. 10 is substantial, a result of the relatively long nuclear absorption length for positive kaons. As a result of the difference (λ^{K^+} is 19%–66% less than λ^{K^-}, λ^{π^+}, or λ^{π^-} based on GHEISHA and FLUKA values shown in Table III) the PHENIX muon arm steel presents 1.1–4.5 fewer interaction lengths to positive kaons than other hadron species.

G. Background tracks

The main source of tracks which are not accounted for in the yield of punchthrough hadrons and free-decay muons, and which are not due to vertex-independent muons, are light hadrons which penetrate through the pre-MuTR absorber, decay into a muon, and are still reconstructed as a valid track.

A simulation of single pions thrown into the muon arm acceptance shows that the number of hadrons which decay after the pre-MuTR absorber and penetrate to MuID gap 4 is only 5%–10% (increasing with increasing p_T) of the z_{vtx}-averaged number of free-decay muons, $N_D(p_T, z_{vtx} = 0)$. This ratio will be suppressed by the fact that tracks which decay are less likely to be reconstructed successfully. It is further suppressed by our punchthrough calculation procedure: the number of such tracks which stop in MuID gap 3 is roughly half the number that penetrate to gap 4; these will be counted in our calculation of the punchthrough hadron yield.

We express our estimate for the yield of background tracks not otherwise accounted for as $N_B(p_T) = 5\% \times N_D(p_T, z_{vtx} = 0)$. The systematic uncertainty assigned to this quantity, $\sigma_{R_B} = 5\% \times N_D(p_T, z_{vtx} = 0)$, covers the extreme possibilities that the N_B/N_D is unsuppressed or fully suppressed by reconstruction and punchthrough procedures, as described above (see Table VIII).

This estimate was verified in a simulation of π^-'s and K^-'s which were thrown into the muon arm acceptance and fully reconstructed. The reconstructed track information, together with the Monte Carlo truth information, allows us to eliminate uncertainties due to misreconstruction of the track p_T and due to determination of whether a track which penetrated to the last gap did so in a reconstructible fashion.

H. Vertex-independent muons

Figure 11 shows the yield of inclusive muon candidates, $N_I(p_T, z_{vtx})$, with contributions from individual components (free-decay muons, punchthrough hadrons, and background tracks) shown as well as their sum. The vertex-independent muons can be seen as the clear excess above the calculated background sources. The systematic error bands shown on the component sums are discussed in Sec. III I and listed in Tables VI and VII.

We obtain the yield of vertex-independent muons by applying Eq. (2) in each p_T bin, subtracting the hadronic contributions from the inclusive muon candidate yield, and averaging over z_{vtx} bins. This yield is shown, before averaging over z_{vtx} to demonstrate the expected vertex independence, in Fig. 12.

We make one final correction for momentum scale. The observed mass of the J/ψ, reconstructed with the same code and in the same data set, is higher than the nominal value by ≈ 100 MeV(3%) [51]. However, in a higher

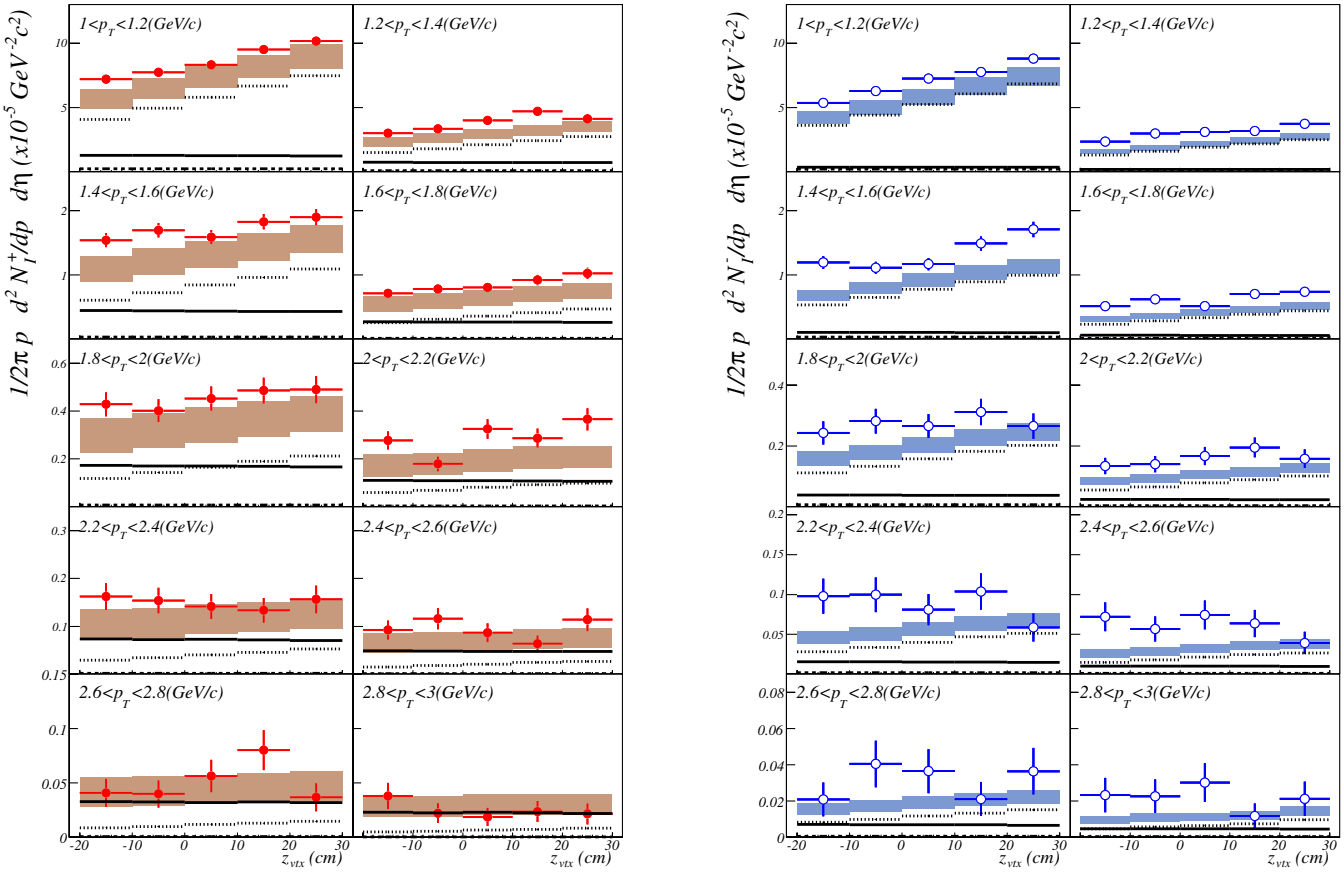

FIG. 11 (color online). Points show the yield of (left) positively and (right) negatively charged inclusive muon candidates vs z_{vtx} for different p_T bins with statistical errors. Dotted, solid, and dashed lines show contributions from decay muons, punchthrough hadrons, and background tracks, respectively. Shaded bands show the systematic error around the sum of these components, as listed in Tables V, VI, and VII and discussed in Sec. III I. The larger systematic uncertainties for positive particles are due to the larger fractional contribution of punchthrough background, which in turn is due to the relatively long nuclear interaction cross section for positive kaons.

statistics data set the momentum scale accuracy is verified to within 1% by our observation of the accepted value for the mass of the J/ψ [52]. Also, the peak observed in the longitudinal momentum distribution of particles stopping in MuID gap 3 (see Fig. 8) is within 0.5% of the predicted value. We therefore assume that the momentum scale is high by 1.5% (splitting the difference between 0 and 3%). This results in a momentum scale correction factor to the prompt muon yield of $0.94 + 0.987 \times (p_T[\mathrm{GeV}/c] - 1)$. We assume a 100% systematic error on this correction factor, as shown in Table V.

Finite momentum resolution can cause a similar effect. Contributions from energy-loss fluctuations, multiple scattering, and chamber resolution combine to give $\delta p/p \approx 5\%$ for the momentum range used in this analysis. Finite resolution, combined with an exponentially falling spectrum, artificially hardens the measured spectrum. For $1 < p_T < 3$ GeV/c this hardening increases the normalization of the yield by 3.7%. However, this is accounted for in our efficiency determination since we use a realistic p_T spectrum as input. Therefore, we apply no explicit correction and no additional systematic uncertainty for this effect.

The final values for the vertex-independent muon cross section, obtained from Eq. (3), are shown in Fig. 13. Points in this figure have been placed at the average p_T value of the bin contents to account for bin shifting in the steeply falling distributions. Systematic errors shown in this figure are discussed in Sec. III I and listed in Tables V, VI, and VII.

I. Systematic errors

Many sources of systematic error on the yield of vertex-independent muons, N_μ, are common to the different components of the inclusive muon candidate yield. In order to account for this we rewrite Eq. (2) (making the p_T and z_{vtx} dependencies implicit) as:

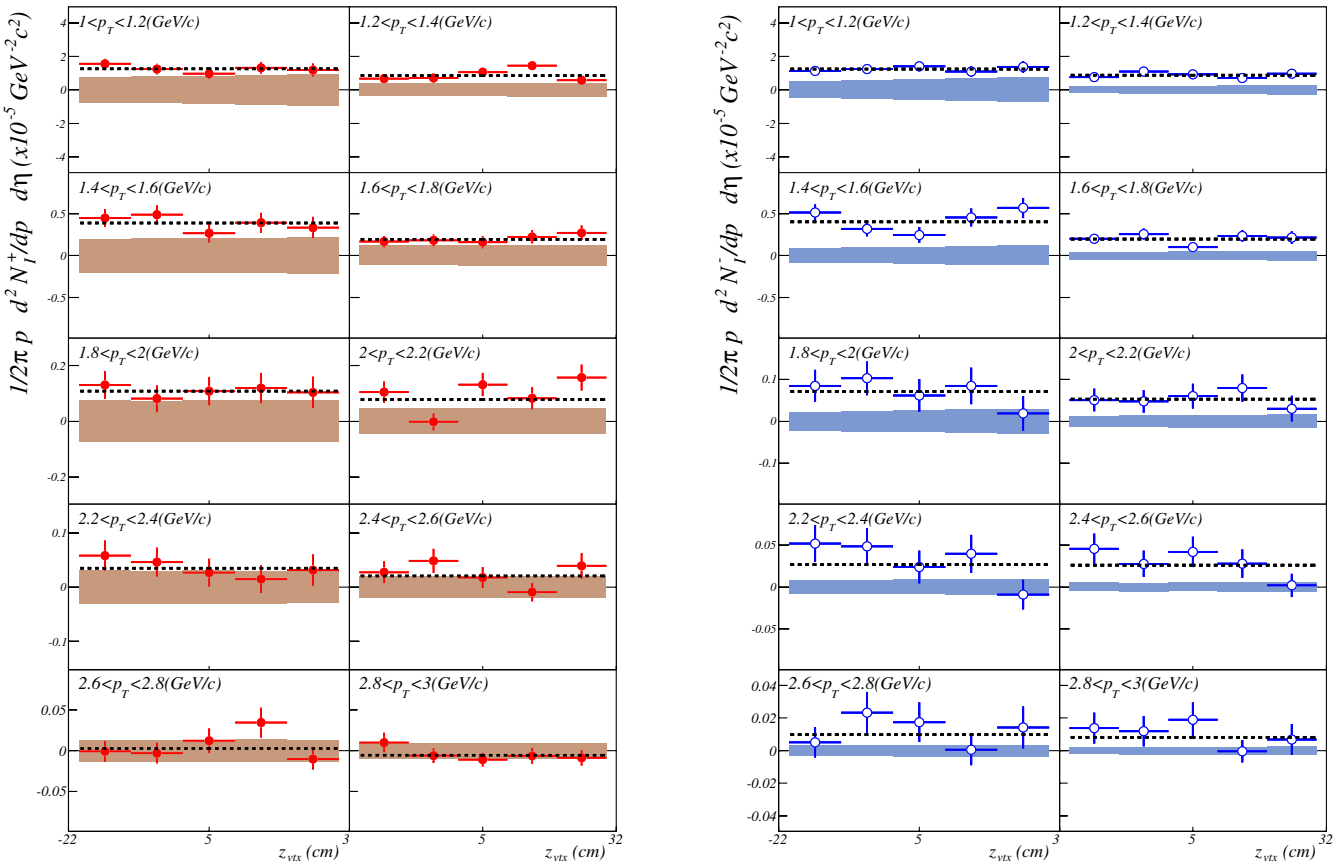

FIG. 12 (color online). Points show the yield of (left) positively and (right) negatively charged vertex-independent muons vs z_{vtx} for different p_T bins with statistical errors. The dashed lines show the yield for each p_T bin, averaged over z_{vtx}. The shaded bands around 0 show the systematic error on the sum of the contributions to the inclusive muon candidate yield from light-hadronic sources, as listed in Tables V, VI, and VII and discussed in Sec. III I. The larger systematic uncertainties for positive particles are due to the larger fractional contribution of punchthrough background, which in turn is due to the relatively long nuclear interaction cross section for positive kaons.

$$\begin{aligned} N_\mu &= N_I \times (N_\mu/N_I) \\ &= N_I \times ((N_I - N_D - N_P - N_B)/N_I) \\ &= N_I \times (1 - R_D - R_P - R_B), \end{aligned} \tag{12}$$

where $R_j = N_j/N_I$ is the fraction of the inclusive muon candidate yield attributed to the j^{th} component. We can now write the systematic error on N_μ as:

$$\sigma_{N_\mu} = \sqrt{(\sigma_{N_I}/N_I)^2 N_\mu^2 + (\sigma_{R_D}^2 + \sigma_{R_P}^2 + \sigma_{R_B}^2) N_I^2} \tag{13}$$

σ_{N_μ}, as determined below, is displayed in Figs. 11 and 12.

Note that the uncertainties for positive particles are significantly larger than for negative particles. This is due to the fact that the fraction of the inclusive muon candidate yield from punchthrough background is significantly larger for positive particles than for negative particles, as shown in Fig. 10. As discussed above, this is due to the relatively long nuclear interaction cross section for positive kaons.

Uncertainties contributing to σ_{N_I} are listed in Table V. Uncertainties contributing to σ_{N_D} and σ_{R_D} are listed in Table VI. Uncertainties contributing to σ_{N_P} and σ_{R_P} are listed in Table VII. Note that in these tables we separately list uncertainties that affect the overall normalization (σ/N^{norm}) and the shape of the p_T spectrum (σ/N^{p_T}).

TABLE V. Sources of systematic error on the calculation of N_I, the yield of inclusive muon candidates. σ_{N_I}/N_I is obtained by adding the different contributions in quadrature.

Error source	σ/N^{norm}	σ/N^{p_T}
Momentum scale	6.0%	$(p_T[\text{GeV}/c] - 1) \times 1.3\%$
ε_{acc}	10%	$(p_T[\text{GeV}/c] - 1) \times 1.5\%$
ε_{rec}	9.0%	0
$\varepsilon_{\text{user}}$	5.0%	$(p_T[\text{GeV}/c] - 1) \times 5.0\%$
$\varepsilon_{\text{trig}}$	4.7%	0
σ_{N_I}/N_I	16.3%	$(p_T[\text{GeV}/c] - 1) \times 5.4\%$

TABLE VI. Sources of systematic error on R_D, the ratio of free-decay muons to inclusive muon candidates, and N_D, the absolute yield of free-decay muons. σ_{R_D} is obtained by adding the different contributions in quadrature. σ_{N_D}/N_D is obtained by adding σ_{R_D} and σ_{N_I}/N_I in quadrature.

Error source	σ/N^{norm}	σ/N^{p_T}
Decay flight path	5%	0
z_{vtx} fit range	3.3%	0
Input hadron spectrum	0	$(p_T[\text{GeV}/c]-1)\times 5.0\%$
Decay normalization	7%	0
σ_{R_D}	9.2%	$(p_T[\text{GeV}/c]-1)\times 5.0\%$
σ_{N_D}/N_D	18.7%	$(p_T[\text{GeV}/c]-1)\times 7.4\%$

TABLE VII. Sources of systematic error on R_P, the ratio of punchthrough hadrons to inclusive muon candidates, and N_P, the absolute yield of punchthrough hadrons. σ_{R_P} is obtained by adding the different contributions in quadrature. σ_{N_P}/N_P is obtained by adding σ_{R_P} and σ_{N_I}/N_I in quadrature.

Error source	σ/N^{norm}	σ/N^{p_T}
$\varepsilon^3_{\text{scale}}$	23%	0
Exponential absorption model	0	32%
p and $\bar{p}$ contributions	10%	0
N_3^{stop} normalization	10%	0
σ_{R_P}	27%	32%
σ_{N_P}/N_P	31.5%	$\approx 32\%$

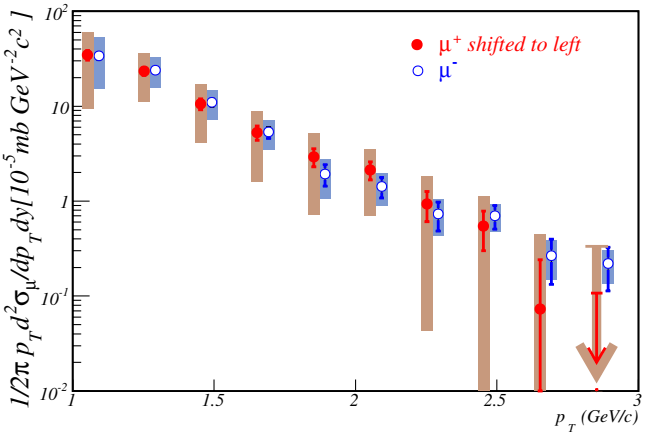

FIG. 13 (color online). p_T spectrum of vertex-independent muons. Error bars indicate statistical errors. One point with unphysical (less than zero) extracted yield is shown as an arrow pointing down from the 90% C.L. upper limit Shaded bands indicate systematic errors, as listed in Tables V, VI, and VII and discussed in Sec. III I. The larger systematic uncertainties for positive particles is due to the larger fractional contribution of punchthrough background, which in turn is due to the relatively long nuclear interaction cross section for positive kaons.

TABLE VIII. Other sources of systematic uncertainty. σ_{R_B} is incorporated into the systematic uncertainty on the vertex-independent muon yield, as shown in Eq. (13). Errors on σ^{pp}_{BBC} and $\varepsilon^{c,\bar{c}\to\mu}_{\text{BBC}}$ are added in quadrature along with the total uncertainty on the vertex-independent muon yield, σ_{N_μ}/N_μ to get the uncertainty on the vertex-independent muon cross section.

Error source	σ/N^{norm}	σ/N^{p_T}
σ_{R_B}	0	$5\%\times N_D(p_T, z_{vtx}=0)$
$\sigma_{\sigma^{pp}_{\text{BBC}}}$	9.6%	0
$\sigma_{\varepsilon^{c,\bar{c}\to\mu}_{\text{BBC}}}$	5%	0

Values for σ_{N_I}/N_I are displayed in Fig. 6. Values for σ_{R_D} and σ_{R_P} are displayed in Figs. 7 and 10 respectively. We insert σ_{N_I}/N_I, σ_{R_D}, σ_{R_P}, and σ_{R_B} into Eq. (13) as part of the final systematic error on N_μ.

To get the vertex-independent muon cross section, as defined in Eq. (3) and displayed in Figs. 13 and 16, we need to add in quadrature the errors on N_μ, σ^{pp}_{BBC}, $\varepsilon^{c,\bar{c}\to\mu}_{BBC}$. The error on N_μ is obtained from the components above according to Eq. (13). Errors on σ^{pp}_{BBC} and $\varepsilon^{c,\bar{c}\to\mu}_{BBC}$ are listed in Table VIII.

IV. CHARM CROSS SECTION

The charm production cross section obtained from the yield of vertex-independent muons (or from the yield of nonphotonic electrons, or D mesons) is necessarily model dependent since we do not measure the charm quarks directly. We use PYTHIA to convert our measurement of the vertex-independent muon yield into an estimate of the differential charm production cross section at forward rapidity, $d\sigma_{c\bar{c}}/dy|_{y=1.6}$, in a procedure very similar to that used in PHENIX measurements of charm production at $y=0$ [7–13]. We use PYTHIA version 6.205 with parameters tuned to reproduce charm production data at SPS and FNAL [71] and single-electron data at the ISR [72–74]. Tuned parameters are listed in Table VIII. The meaning of each parameter is more thoroughly defined in the PYTHIA manual [75].

Vertex-independent muon sources, predicted by a PYTHIA simulation using the same parameters (except that MSEL is set to 2 to generate unbiased collisions), are listed in Table X. These sources include decays of hadrons containing a heavy quark, and light-vector mesons with a decay length too short to be measured with the existing experimental apparatus (ρ, ω, ϕ). Their p_T spectra are shown in Fig. 14. Contributions from quarkonium decays, Drell-Yan, and τ lepton decays are negligible. This shows that vertex-independent muon production in our acceptance is dominated by muons from decay of charm hadrons, although for $p_T > 2.5$ GeV/c the contribution from decays of hadrons containing a bottom quark is starting to become significant.

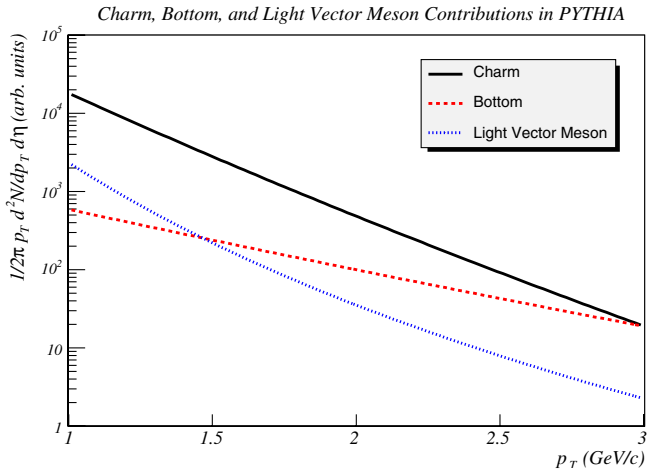

FIG. 14 (color online). PYTHIA calculation showing the major contributions to the vertex-independent muon p_T spectrum. Solid, dashed, and dotted lines show the yield from charm, bottom, and light vector mesons (ρ, ω, ϕ), respectively.

This simulation also gives the distribution of charm quarks (p_T vs y) that produce a muon in our acceptance, as shown in Fig. 15. This demonstrates that the vertex-independent muons we measure sample charm quarks down to $p_T \approx 1$ GeV/c, over a narrow rapidity slice centered at $y = 1.6$.

Figure 16 shows a comparison of the measured vertex-independent negative muon spectrum (from Fig. 13) to the prediction of this default PYTHIA simulation and to a FONLL calculation [20,77]. Note, larger systematic errors for the positive muon spectrum preclude a significant measurement for that charge sign. One can see that the measured values significantly exceed both predictions. The spectrum also appears to be somewhat harder than the PYTHIA spectrum with the parameters listed in Table IX.

We scale the charm (only) contribution to the PYTHIA vertex-independent muon p_T spectrum such that the total

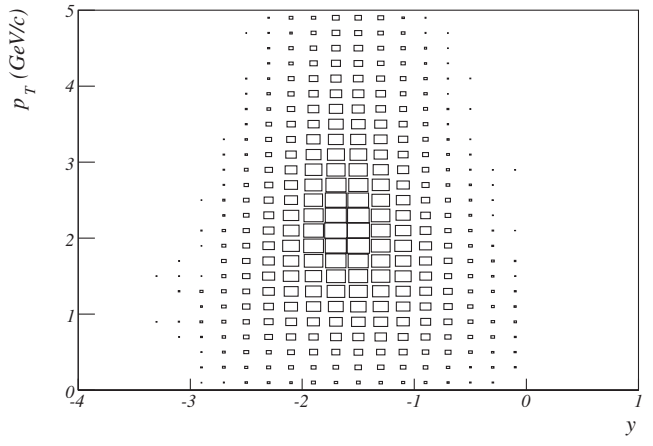

FIG. 15. PYTHIA results for the p_T vs y distribution (linear z-scale) of charm quarks that produce a muon in the PHENIX acceptance.

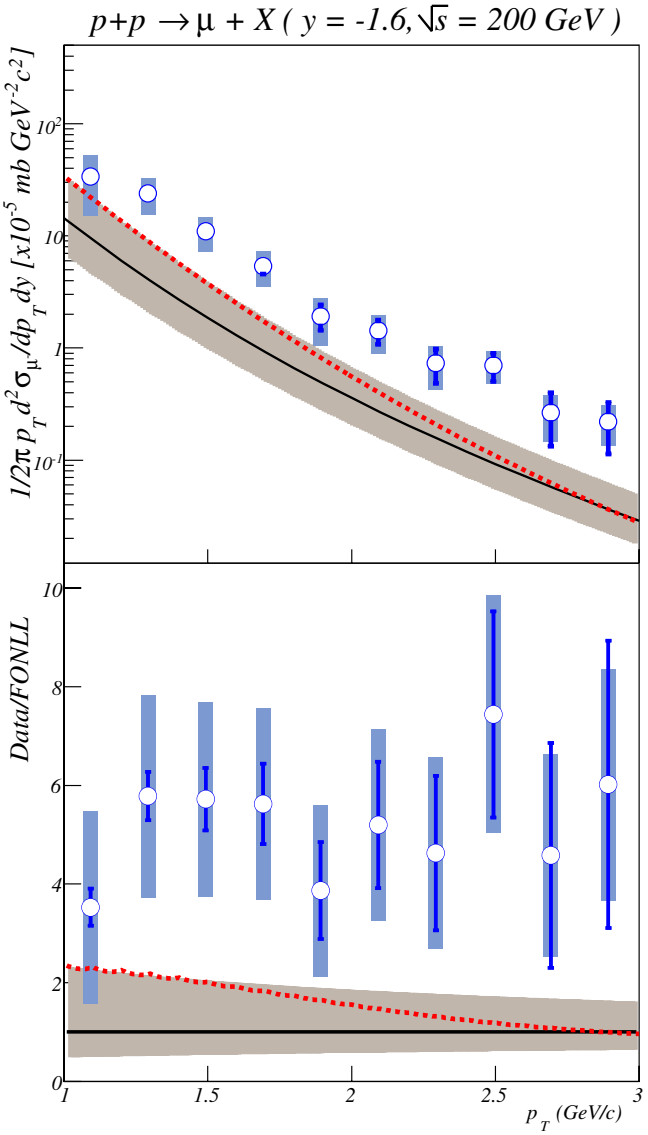

FIG. 16 (color online). The top panel shows the measured p_T spectrum of vertex-independent negative muons from Fig. 13, the PYTHIA prediction using settings listed in Table IX without scaling the charm contribution (dotted line), and a FONLL calculation (solid line with systematic error band) [20,77]. The bottom panel shows the ratio of the measured spectrum to the FONLL calculation with statistical (error bars) and systematic (bands) uncertainties on the data, as well as the theoretical uncertainty (shaded band around 1). The dashed line shows the PYTHIA/FONLL ratio.

spectrum (including the small contributions from open bottom and vector mesons) matches the central values of the measured vertex-independent negative muon spectrum. Only statistical errors are used in the fit. We multiply the scale factor from the fit (2.27) by the PYTHIA value for the charm production cross section, $d\sigma_{c\bar{c}}/dy|^{\mathrm{PYTHIA}}_{y=1.6}$ (0.107 mb), to obtain $d\sigma_{c\bar{c}}/dy|^{\mathrm{PHENIX}}_{y=1.6} = 0.243 \pm 0.013(\mathrm{stat.})$ mb.

TABLE IX. Tuned PYTHIA parameters (default settings for this analysis) for determination of charm production cross section central value.

Parameter	Value	Meaning
MSEL	4	Heavy quark production every event (gluon fusion + $q/\bar{q}$ annihilation).
MSTP (32)	4	Hard scattering scale, $Q^2 = \hat{s}$.
MSTP (33)	1	Use K-factor.
MSTP (52)	2	Use PDF libraries.
MSTP (51)	4046	Select CTEQ5L PDF libraries [76].
MSTP (91)	1	Use Gaussian distribution for intrinsic k_T.
PARP (31)	3.5	K-factor.
PARP (91)	1.5	$\langle k_T \rangle$ (GeV/c).
PARP (93)	5.0	Maximum k_T (GeV/c).
PMAS (4, 1)	1.25	m_c (GeV/c).
D^+/D^0	0.32	Default charm chemistry ratio.

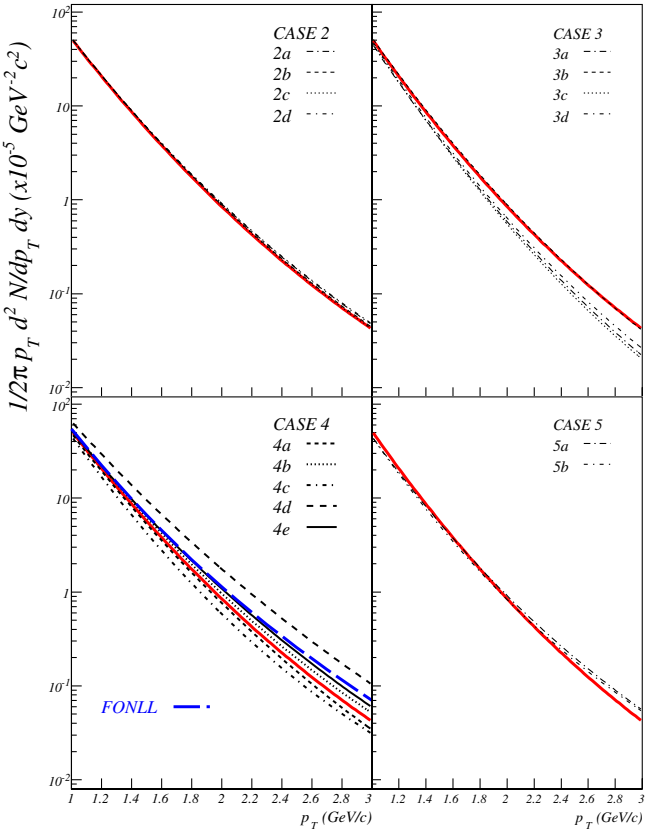

FIG. 17 (color online). PYTHIA results with different parameter sets for the negative vertex-independent muon p_T spectrum per event in which a $c\bar{c}$ pair is created. The solid line in each panel shows the result when using default settings listed in Table IX. Legends indicate the correspondence between line style and the simulation case label. Parameter sets for each case label are given in Table XI.

TABLE X. Percentage contribution of different sources of vertex-independent muons within our acceptance ($1 < p_T < 3$ GeV/c and $1.5 < |\eta| < 1.8$), from PYTHIA, with parameters listed in Table IX (except that MSEL = 2 to generate minimum bias collisions).

Source	Contribution
Open charm	84.6%
Open bottom	6.9%
ρ, ω, ϕ	8.1%
Quarkonia	<0.1%
Drell-Yan	<0.1%
τ leptons	0.4%

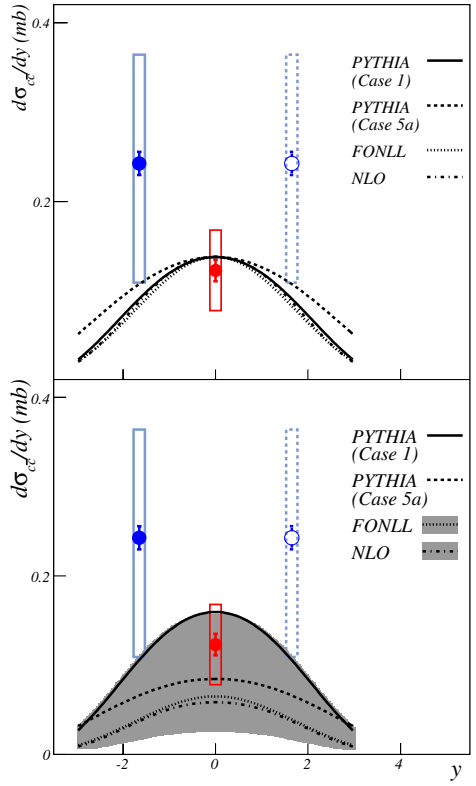

FIG. 18 (color online). Comparisons of measured charm rapidity distributions, $d\sigma_{c\bar{c}}/dy$ vs y, to theoretical predictions. Data points at $y = \pm 1.6$ are from this analysis (the point at $y = 1.6$ is reflected through $y = 0$). The point at $y = 0$ is the PHENIX measurement of charm through semileptonic decay to electrons [13]. Error bars on the data points indicate statistical uncertainties and boxes indicate systematic uncertainties. The top panel shows rapidity spectra from two PYTHIA parameter sets (see Table XI for details), FONLL [20,77], and a NLO calculation [83]. The PYTHIA curve with the default parameter set (case 1) was fit to the two PHENIX data points with statistical and systematic errors added in quadrature. All other theory curves were normalized so that they are equal at $y = 0$ to allow shape comparisons. The bottom panel shows the theory curves without normalization. Theoretical uncertainties associated with the FONLL and NLO calculations are indicated with shaded bands.

TABLE XI. Results for PYTHIA simulations with different parameter sets used to explore the systematic error on the charm cross section due to model uncertainties. The top of the table details the different parameter sets tested. Unless otherwise noted, parameters are the same as those listed in Table IX. The bottom of the table gives the results for different simulations: The first column identifies the simulation; the second column gives the total charm production cross section given the chosen PYTHIA parameter set; the third column gives the differential charm production cross section at $y = 1.6$; the fourth column gives the normalization factor needed to fit the PHENIX data; the fifth column gives the differential charm production cross section at $y = 1.6$ for PHENIX data (the product of the third and fourth columns); the sixth column gives the fractional difference between the results for each simulation compared to the simulation with the default PYTHIA parameter set; the last column gives the ratio $d\sigma_{c\bar{c}}/dy|^{\mathrm{PYTHIA}}_{y=1.6}/d\sigma_{c\bar{c}}/dy|^{\mathrm{PYTHIA}}_{y=0}$.

Case	PYTHIA Settings
1	Default settings, see Table IX.
2a	MSTP(51) = 4032, CTEQ4L PDF libraries [78].
2b	MSTP(51) = 5005, GRV94LO PDF libraries [79].
2c	MSTP(51) = 5012, GRV98LO PDF libraries [80].
2d	MSTP(51) = 3072, MRST (c−g) PDF libraries [81].
3a	MSTP(32) = 1, $Q^2 = 2\hat{s}\,\hat{t}\,\hat{u}/(\hat{s}^2 + \hat{t}^2 + \hat{u}^2)$.
3b	MSTP(32) = 2, $Q^2 = p_T^2 + (m_3^2 + m_4^2)/2$.
3c	MSTP(32) = 3, $Q^2 = \min(-\hat{t}, -\hat{u})$.
3d	MSTP(32) = 5, $Q^2 = -\hat{t}$.
4a	PMAS(4, 1) = $m_c = 1.15$ GeV/c.
4b	PMAS(4, 1) = $m_c = 1.35$ GeV/c.
4c	PARP(91) = $\langle k_T \rangle = 0.3$ GeV/c.
4d	PARP(91) = $\langle k_T \rangle = 3.0$ GeV/c.
4e	MSTP(68) = 2, Maximum virtuality scale and matrix element matching scheme. PARP(67) = 4, Multiplicative factor applied to hard scattering scale.
5a	PARP(31) = K-factor = 1, MSEL = 1, Hard scattering enabled.
5b	PARP(31) = K-factor = 1, MSEL = 1, Hard scattering enabled, All other parameters untuned.
6	$D^+/D^0 = 0.45$ [82].
7	Open bottom and vector mesons scale with charm.

Case	$\sigma_{c\bar{c}}^{\mathrm{PYTHIA}}$ (mb)	$d\sigma_{c\bar{c}}/dy\|^{\mathrm{PYTHIA}}_{y=1.6}$ (mb)	Normalization to Data	$d\sigma_{c\bar{c}}/dy\|^{\mathrm{PHENIX}}_{y=1.6}$ (mb)	$\Delta d\sigma_{c\bar{c}}/dy\|^{\mathrm{PHENIX}}_{y=1.6}$ (%)	$d\sigma_{c\bar{c}}/dy\|^{\mathrm{PYTHIA}}_{y=1.6}/d\sigma_{c\bar{c}}/dy\|^{\mathrm{PYTHIA}}_{y=0}$
1	0.658	0.107	2.27	0.243	—	0.67
2a	0.691	0.111	2.10	0.232	−4.5	0.69
2b	0.698	0.112	2.09	0.233	−3.9	0.71
2c	0.669	0.109	2.18	0.238	−1.7	0.73
2d	0.551	0.088	2.67	0.236	−2.9	0.71
3a	1.520	0.243	1.12	0.271	11.8	0.84
3b	0.863	0.139	1.63	0.226	−6.7	0.71
3c	1.501	0.242	1.11	0.267	10.2	0.84
3d	1.104	0.178	1.45	0.258	6.4	0.78
4a	0.905	0.145	1.73	0.252	3.7	0.67
4b	0.487	0.078	2.91	0.226	−6.7	0.64
4c	0.658	0.104	2.81	0.292	20.4	0.66
4d	0.658	0.104	1.50	0.156	−35.8	0.63
4e	0.658	0.106	2.09	0.220	−9.2	0.63
5a	0.435	0.068	3.91	0.266	9.4	0.80
5b	0.385	0.058	4.67	0.271	11.7	0.79
6	0.658	0.107	2.38	0.255	5.0	0.67
7	0.658	0.107	2.20	0.236	−2.9	0.67

We distinguish between two different sources of systematic uncertainty on the extraction of the charm cross section: (1) uncertainty in the PYTHIA calculation and (2) uncertainty in the data, which is largely independent of PYTHIA.

We determined the uncertainty in the data ($\pm$ 43%) by refitting PYTHIA to the data at the minimum and maximum of the 1σ systematic error band.

We determined the uncertainty in the PYTHIA calculation with a systematic study in which we varied simulation parameters, extracted the new simulated vertex-independent negative muon spectrum, normalized to the measured spectrum, and extracted $d\sigma_{c\bar{c}}/dy|_{y=1.6}^{\mathrm{PHENIX}}$ for the modified parameter sets. We varied PDF libraries, the hard scattering scale, the charm quark mass, the intrinsic k_T value, the D^+/D^0 ratio, charm production mechanism selections, and open bottom and vector meson scaling assumptions. The parameter sets used and the results of this study are summarized in Table XI.

The PYTHIA charm cross section varies substantially ($\Delta(d\sigma_{c\bar{c}}/dy)|_{y=1.6}^{\mathrm{PYTHIA}}) \approx 4$) for the chosen parameter sets. However, the extracted experimental charm cross section is relatively stable ($\Delta(d\sigma_{c\bar{c}}/dy)|_{y=1.6}^{\mathrm{PHENIX}} < 0.36$). This is due to the fact that the parameter set changes have relatively minor effects on the shape of the predicted vertex-independent muon p_T spectrum, and we obtain the experimental charm cross section by normalizing the PYTHIA charm cross section by the ratio of the measured and predicted muon p_T spectra.

One way to visualize this is to plot (see Fig. 17) the vertex-independent muon yield in our acceptance per event in which a $c\bar{c}$ pair is created for the different PYTHIA parameter sets. Because of our procedure, parameter sets which give similar vertex-independent muon yields per $c\bar{c}$ event in the low p_T region (which dominates the fit) will necessarily give similar values for $d\sigma_{c\bar{c}}/dy|_{y=1.6}^{\mathrm{PHENIX}}$, whatever the PYTHIA charm cross section is.

The largest variation in the predicted muon yield at $p_T = 1$ GeV/c per $c\bar{c}$ event is seen for simulations in which the intrinsic k_T is varied from its default value ($\langle k_T \rangle = 1.5$ GeV/c) to the value expected from arguments based on Fermi momentum (case 4c, $\langle k_T \rangle = 0.3$ GeV/c), or to a value which best reproduces the measured spectrum at higher p_T (case 4d, $\langle k_T \rangle = 3.0$ GeV/c). These parameter sets also result in the largest variation in $d\sigma_{c\bar{c}}/dy|_{y=1.6}^{\mathrm{PHENIX}}$, as shown in Table X. We use the cross section values obtained in this pair of simulations to define the systematic uncertainty in our measurement due to the uncertainty in our PYTHIA calculation. This gives us our final answer: $d\sigma_{c\bar{c}}/dy|_{y=1.6} = 0.243 \pm 0.013(\mathrm{stat.}) \pm 0.105(\mathrm{datasyst.})^{+0.049}_{-0.087}(\mathrm{PYTHIAsyst.})$ mb. As shown in the lower-left panel of Fig. 17, the FONLL prediction of the muon yield per $c\bar{c}$ collision lies well within the extreme cases defining the systematic error resulting from the necessary model dependence of our charm extraction. Therefore, using FONLL instead of PYTHIA for the charm extraction would yield consistent results.

Figure 18 shows the PHENIX charm rapidity spectrum. The result of this analysis (mirrored about $y = 0$ since this is a symmetric collision system) is plotted along with the result for $d\sigma_{c\bar{c}}/dy|_{y=0}$ [13]. In order to compare with the data at $y = 0$ the systematic uncertainty on the data from this analysis is shown as the quadrature sum of the two sources of systematic uncertainty described above (data and PYTHIA). Theoretical curves from PYTHIA (case 1 and case 5a), FONLL [20,77], and a NLO calculation from Vogt [83] are also displayed.

In the top panel of the figure PYTHIA with the default parameter set (case 1) is fit to the two PHENIX points with statistical and systematic errors added in quadrature. Other theory curves are normalized so that they are equal at $y = 0$ in order to allow shape comparisons. As shown in Table XI, different PYTHIA parameter sets differ in the predicted ratio $d\sigma_{c\bar{c}}/dy|_{y=1.6}^{\mathrm{PYTHIA}}/d\sigma_{c\bar{c}}/dy|_{y=0}^{\mathrm{PYTHIA}}$ by $>30\%$. Unfortunately, current systematic error bars preclude any conclusions about the charm production rapidity shape.

In the bottom panel of the figure the theory curves are without normalization to allow an absolute comparison. The quoted theoretical uncertainty bands for the FONLL and NLO calculations are also shown. We note that, although our data are above the FONLL prediction, the error bars touch. This is in contrast to the situation for the vertex-independent muon cross section, shown in Fig. 16, where the data are significantly above the prediction. The larger disagreement in the vertex-independent muon cross section is presumably due to different treatment of the fragmentation process in PYTHIA and FONLL [20,77,83].

V. CONCLUSION AND OUTLOOK

We have measured muon production at forward rapidity ($1.5 \leq |\eta| \leq 1.8$), in the range $1 < p_T < 3$ GeV/c, in $\sqrt{s} = 200$ GeV $p + p$ collisions at RHIC. We determined and subtracted the contribution from light hadron sources (π, K, p) to obtain the vertex-independent muon yield which, for the p_T range measured in this analysis, and in the absence of new physics, arises dominantly from the decay of D mesons. We normalized the PYTHIA muon spectrum resulting from the production of charm quarks to obtain the differential cross section for charm production at forward rapidity: $d\sigma_{c\bar{c}}/dy|_{y=1.6} = 0.243 \pm 0.013(\mathrm{stat.}) \pm 0.105(\mathrm{datasyst.})^{+0.049}_{-0.087}(\mathrm{PYTHIAsyst.})$ mb. This is compatible with PHENIX charm measurement at $y = 0$, although even further above predictions from PYTHIA and FONLL. Large systematic uncertainties in the current measurement preclude statements about the rapidity dependence of the charm cross section.

The systematic uncertainty in the data is dominated by uncertainty on the determination of the fractional contribution of decay muons. This will be improved with higher

statistics data sets (already collected) which will allow better measurements of the z_{vtx} dependence of particle production. Final results for identified particle p_T distributions in $p + p$ collisions by BRAHMS will also be invaluable for improving the input to our hadron generator. The systematic uncertainty in PYTHIA is dominated by differences observed when the intrinsic $\langle k_T \rangle$ is varied. In order to reduce this uncertainty we need to reduce the allowed parameter space by improving the measurement of the high p_T portion of the vertex-independent muon spectrum, where the error is dominated by the uncertainty in the yield of punchthrough hadrons. Data sets (already collected) with higher statistics, and with hadrons stopping in MuID gap 2, will allow a completely data-driven approach to the calculation of the punchthrough yield. This will eliminate the reliance on hadronic interaction simulation packages, differences in which are the largest source of systematic error at high p_T. Analogous measurements are also being carried out for $d + Au$, $Cu + Cu$, and $Au + Au$ [84] collisions at $\sqrt{s_{NN}} = 200$ GeV. These will allow determination of the magnitude of nuclear modification effects on charm production at forward rapidity.

ACKNOWLEDGMENTS

We thank the staff of the Collider-Accelerator and Physics Departments at Brookhaven National Laboratory and the staff of the other PHENIX participating institutions for their vital contributions. We acknowledge support from the Department of Energy, Office of Science, Nuclear Physics Division, the National Science Foundation, Abilene Christian University Research Council, Research Foundation of SUNY, and Dean of the College of Arts and Sciences, Vanderbilt University (USA), Ministry of Education, Culture, Sports, Science, and Technology and the Japan Society for the Promotion of Science (Japan), Conselho Nacional de Desenvolvimento Científico e Tecnológico and Fundação de Amparo à Pesquisa do Estado de São Paulo (Brazil), Natural Science Foundation of China (People's Republic of China), Centre National de la Recherche Scientifique, Commissariat à l'Énergie Atomique, Institut National de Physique Nucléaire et de Physique des Particules, and Institut National de Physique Nucléaire et de Physique des Particules (France), Bundesministerium für Bildung und Forschung, Deutscher Akademischer Austausch Dienst, and Alexander von Humboldt Stiftung (Germany), Hungarian National Science Fund, OTKA (Hungary), Department of Atomic Energy and Department of Science and Technology (India), Israel Science Foundation (Israel), Korea Research Foundation and Korea Science and Engineering Foundation (Korea), Russian Ministry of Industry, Science and Tekhnologies, Russian Academy of Science, Russian Ministry of Atomic Energy (Russia), V. R. and the Wallenberg Foundation (Sweden), the U.S. Civilian Research and Development Foundation for the Independent States of the Former Soviet Union, the US-Hungarian NSF-OTKA-MTA, the US-Israel Binational Science Foundation, and the 5th European Union TMR Marie-Curie Programme.

[1] B. Abbott *et al.* (D0 Collaboration), Phys. Rev. Lett. **84**, 5478 (2000).
[2] D. Acosta *et al.* (CDF Collaboration), Phys. Rev. D **71**, 032001 (2005).
[3] M. Cacciari, arXiv:hep-ph/0407187.
[4] M. Cacciari, M. Greco, and P. Nason, J. High Energy Phys. 05 (1998) 007.
[5] M. L. Mangano, AIP Conf. Proc. **753**, 247 (2005).
[6] D. Acosta *et al.* (CDF Collaboration), Phys. Rev. Lett. **91**, 241804 (2003).
[7] K. Adcox *et al.* (PHENIX Collaboration), Phys. Rev. Lett. **88**, 192303 (2002).
[8] S. S. Adler *et al.* (PHENIX Collaboration), Phys. Rev. Lett. **94**, 082301 (2005).
[9] S. S. Adler *et al.* (PHENIX Collaboration), Phys. Rev. Lett. **96**, 032001 (2006).
[10] S. Kelly (PHENIX Collaboration), J. Phys. G **30**, S1189 (2004).
[11] S. S. Adler *et al.* (PHENIX Collaboration), Phys. Rev. Lett. **96**, 032301 (2006).
[12] S. Butsyk (PHENIX Collaboration), Nucl. Phys. **A774**, 669 (2006).
[13] A. Adare *et al.* (PHENIX Collaboration), Phys. Rev. Lett. **97**, 252002 (2006).
[14] S. S. Adler *et al.* (PHENIX Collaboration), Phys. Rev. C **72**, 024901 (2005).
[15] S. Sakai (PHENIX Collaboration), J. Phys. G **32**, S551 (2006).
[16] A. Adare *et al.* (PHENIX Collaboration), to be published.
[17] J. Adams *et al.* (STAR Collaboration), Phys. Rev. Lett. **94**, 062301 (2005).
[18] B. I. Abelev *et al.* (STAR Collaboration), Phys. Rev. Lett. **98**, 192301 (2007).
[19] T. Sjöstrand *et al.*, Comput. Phys. Commun. **135**, 238 (2001).
[20] M. Cacciari, P. Nason, and R. Vogt, Phys. Rev. Lett. **95**, 122001 (2005).
[21] M. L. Mangano, Nucl. Phys. **B405**, 507 (1993).
[22] R. Vogt, arXiv:hep-ph/0203151.
[23] R. Vogt, Int. J. Mod. Phys. E **12**, 211 (2003).
[24] W. Cassing, E. Bratkovskaya, and A. Sibirtsev, Nucl. Phys. **A691**, 753 (2001).
[25] E. L. Bratkovskaya, W. Cassing, and H. Stöcker, Phys. Rev. C **67**, 054905 (2003).

[26] C.-Y. Wong, *Introduction to High-Energy Heavy-Ion Collisions* (World Scientific, Singapore, 1994), p. 251.
[27] M. B. Johnson *et al.* (E772 Collaboration), Phys. Rev. Lett. **86**, 4483 (2001).
[28] G. T. Bodwin, S. J. Brodsky, and G. P. Lepage, Phys. Rev. Lett. **47**, 1799 (1981).
[29] G. T. Bodwin, Phys. Rev. D **31**, 2616 (1985).
[30] G. T. Bodwin, S. J. Brodsky, and G. P. Lepage, Phys. Rev. D **39**, 3287 (1989).
[31] B. Z. Kopeliovich and F. Niedermayer, Tech. Rep. E2-84-834, Dubna 1984; http://ccdb3fs.kek.jp/cgi-bin/img/allpdf?198504113.
[32] S. Gavin and J. Milana, Phys. Rev. Lett. **68**, 1834 (1992).
[33] V. Guzey, M. Strikman, and W. Vogelsang, Phys. Lett. B **603**, 173 (2004).
[34] Y. L. Dokshitzer and D. E. Kharzeev, Phys. Lett. B **519**, 199 (2001).
[35] L. McLerran and R. Venugopalan, Phys. Rev. D **49**, 2233 (1994).
[36] L. McLerran and R. Venugopalan, Phys. Rev. D **49**, 3352 (1994).
[37] J. Ashman *et al.* (EMC Collaboration), Phys. Lett. B **202**, 603 (1988).
[38] R. Baier, D. Schiff, and B. Zakharov, Annu. Rev. Nucl. Part. Sci. **50**, 37 (2000).
[39] J. A. Appel, Annu. Rev. Nucl. Part. Sci. **42**, 367 (1992).
[40] B. Müller and X. N. Wang, Phys. Rev. Lett. **68**, 2437 (1992).
[41] T. Matsui and H. Satz, Phys. Lett. B **178**, 416 (1986).
[42] H. Satz, J. Phys. G **32**, R25 (2006).
[43] R. L. Thews and M. L. Mangano, Phys. Rev. C **73**, 014904 (2006).
[44] L. Grandchamp, R. Rapp, and G. E. Brown, Phys. Rev. Lett. **92**, 212301 (2004).
[45] A. Andronic *et al.*, Phys. Lett. B **571**, 36 (2003).
[46] A. P. Kostyuk *et al.*, Phys. Rev. C **68**, 041902(R) (2003).
[47] S. S. Adler *et al.* (PHENIX Collaboration), Phys. Rev. Lett. **94**, 082302 (2005).
[48] I. Arsene *et al.* (BRAHMS Collaboration), Phys. Rev. Lett. **94**, 032301 (2005).
[49] I. Arsene *et al.* (BRAHMS Collaboration), Phys. Rev. Lett. **93**, 242303 (2004).
[50] J. Adams *et al.* (STAR Collaboration), Phys. Rev. Lett. **97**, 152302 (2006).
[51] S. S. Adler *et al.* (PHENIX Collaboration), Phys. Rev. Lett. **92**, 051802 (2004).
[52] S. S. Adler *et al.* (PHENIX Collaboration), Phys. Rev. Lett. **96**, 012304 (2006).
[53] H. Pereira Da Costa (PHENIX Collaboration), Nucl. Phys. **A774**, 747 (2006).
[54] K. Adcox *et al.* (PHENIX Collaboration), Nucl. Instrum. Methods Phys. Res., Sect. A **499**, 469 (2003).
[55] S. S. Adler *et al.* (PHENIX Collaboration), Nucl. Instrum. Methods Phys. Res., Sect. A **499**, 560 (2003).
[56] S. S. Adler *et al.* (PHENIX Collaboration), Nucl. Instrum. Methods Phys. Res., Sect. A **499**, 593 (2003).
[57] M. Allen *et al.* (PHENIX Collaboration), Nucl. Instrum. Methods Phys. Res., Sect. A **499**, 549 (2003).
[58] H. Akikawa *et al.* (PHENIX Collaboration), Nucl. Instrum. Methods Phys. Res., Sect. A **499**, 537 (2003).
[59] S. H. Aronson *et al.* (PHENIX Collaboration), Nucl. Instrum. Methods Phys. Res., Sect. A **499**, 480 (2003).
[60] S. S. Adler *et al.* (PHENIX Collaboration), Phys. Rev. Lett. **91**, 241803 (2003).
[61] GEANT 3.2.1 Manual, CERN W5013 1994; http://wwwasdoc.web.cern.ch/wwwasdoc/pdfdir/geant.pdf.
[62] V. L. Highland, Nucl. Instrum. Methods **129**, 497 (1975).
[63] V. L. Highland, Nucl. Instrum. Methods **161**, 171 (1979).
[64] G. R. Lynch and O. I. Dahl, Nucl. Instrum. Methods Phys. Res., Sect. B **58**, 6 (1991).
[65] S. S. Adler *et al.* (PHENIX Collaboration), Phys. Rev. D (unpublished).
[66] V. Ryabov (PHENIX Collaboration), Nucl. Phys. **A774**, 735 (2006).
[67] S. Eidelman *et al.*, Phys. Lett. B **592**, 1 (2004).
[68] A. Fassò *et al.*, in *Proceedings of the Monte Carlo 2000 Conference, Lisbon, 2000*, edited by A. Kling *et al.* (Springer-Verlag, Berlin, 2001), p. 955; http://www.fluka.org.
[69] H. S. Fesefeldt, Aachen Report No. PITHA 85/02, 1985.
[70] E. W. Cornell *et al.*, Nucl. Instrum. Methods Phys. Res., Sect. A **350**, 150 (1994).
[71] G. A. Alves *et al.* (E769 Collaboration), Phys. Rev. Lett. **77**, 2388 (1996).
[72] F. W. Büsser *et al.*, Nucl. Phys. **B113**, 189 (1976).
[73] P. Perez *et al.*, Phys. Lett. B **112**, 260 (1982).
[74] M. Basile *et al.*, Nuovo Cimento Soc. Ital. Fis. A **65**, 421 (1981).
[75] T. Sjöstrand *et al.*, arXiv:hep-ph/0108264.
[76] H. L. Lai *et al.* (CTEQ Collaboration), Eur. Phys. J. C **12**, 375 (2000).
[77] M. Cacciari (private communication).
[78] H. L. Lai *et al.* (CTEQ Collaboration), Phys. Rev. D **55**, 1280 (1997).
[79] M. Gluck, E. Reya, and A. Vogt, Z. Phys. C **67**, 433 (1995).
[80] M. Gluck, E. Reya, and A. Vogt, Eur. Phys. J. C **5**, 461 (1998).
[81] A. D. Martin *et al.*, Eur. Phys. J. C **23**, 73 (2002).
[82] A. Tai (STAR Collaboration), J. Phys. G **30**, S809 (2004).
[83] R. Vogt (private communication).
[84] X. R. Wang (PHENIX Collaboration), AIP Conf. Proc. **842**, 68 (2006).